Hovudoppgåve

NTNU
Noregs teknisk-naturvitskaplege universitet
Fakultet for medisin og helsevitenskap
Kavliinstitutt for nevrovitenskap

Torstein Slettmoen

Mechanisms of Six-Fold Symmetry in fMRI BOLD-Signal

An Analysis of a Large Grid Cell Dataset

Hovudoppgåve i profesjonsstudiet i medisin
Veileder: May-Britt Moser og Edvard I. Moser

Mai 2020

NTNU
Kunnskap for ei betre verd

Torstein Slettmoen

Mechanisms of Six-Fold Symmetry in fMRI BOLD-Signal

An Analysis of a Large Grid Cell Dataset

Hovudoppgåve i profesjonsstudiet i medisin
Veileder: May-Britt Moser og Edvard I. Moser
Mai 2020

Noregs teknisk-naturvitskaplege universitet
Fakultet for medisin og helsevitenskap
Kavliinstitutt for nevrovitenskap

Table of Contents

Acknowledgements

This thesis was written at the Kavli Institute for Systems Neuroscience and Centre for Neural Computations at the Norwegian University of Science and Technology. The institute is directed by Professor May-Britt Moser and Professor Edvard I. Moser, and mainly conducts science regarding the neural circuits involved in spatial navigation and memory. This project started off as a first meeting with analytical neuroscience for myself back in 2016, where most of my efforts was put into coding in Matlab, something I was completely novel to prior to this project. The project was put on hold for some years until we decided to follow it up in a more thorough and extensive matter, work which resulted in this very thesis. In my time at the institute I have mainly worked on the developmental aspects of the MEC spatial coding, and have worked experimentally with both electrophysiology, optogenetics and calcium imaging. This thesis, however, is the most extensive analytical work I have conducted at the institute.

First of all, I would like to thank my two supervisors May-Britt Moser and Edvard Moser for their encouragement and enthusiasm, and for giving me the opportunity to conduct excellent science with some of the best tools and techniques available, and last but not least with a never-ending goal to understand the brain. The scientific journey I have been so lucky to be a part of during my 5 years in your group has been filled with hard work, struggles and tears of pure joy – and I am looking forward to continuing this work in the following years. Secondly, I would like to thank Torgeir Waaga for introducing me to Matlab and helping with my simple start-up problems and questions, and Trygve Solstad for discussions, ideas and encouragement regarding analyses of the MUA data. Thirdly, I would like to thank Emilie R. Skytøen and Abraham Z. Vollan for fruitful discussions, inspiration, support and many laughs – I look forward for more of them. You are truly one of the main reasons why I enjoy this lab so much. Also, I would also like to thank Vadim Frolov for developing the BNT and support in programming, Ann Mari Amundsgård, Kyrre Haugen, Endre Kråkvik and Haagen Waade for technical support, and all the animal technicians for taking such good care of our animals. Finally, I would like to thank all members of the research group for being good colleagues, for sharing and teaching newcomers their knowledge, and for making the work in the group so inspiring.

Summary

The hippocampal formation's role in spatial navigation and as the brain's internal metric of space has been recognized since the discovery of place cells and grid cells. Through extensive research, mostly conducted in rodents, we know much about these cortical areas' projections, morphology and cellular firing properties. However, how this cortical network encodes a metric of space is not fully understood, and knowledge from human experiments is sparse. Human research is methodologically and ethically more difficult to conduct. Today, the most used measurement of human grid cell activity is hexadirectional differences in fMRI BOLD-signalling in humans exploring a virtual reality environment. The evidence for this signal originating from grid cells comes from electrophysiological cell recordings in rats, but the evidence is inconclusive and has never before been replicated. Replicating this evidence could clarify the reliability of much of today's fMRI research on human grid cell activity. Utilizing single cell recordings could also answer parts of a much bigger question, addressing the cellular mechanisms behind the six-fold symmetry seen in fMRI BOLD-signal during human navigation as well as the mechanism behind the fMRI BOLD-signal itself.

Samandrag

Hippocampusformasjonen si rolle i romleg navigering og som hjernen sitt indre romlege kart har vore annerkjend sidan oppdaginga av stadsceller og gitterceller. Gjennom omfattande forsking, hovudsakleg utført i gnagarar, veit vi mykje om denne kortikale områda sine projeksjonar, morfologi og cellulære fyringseigenskapar. Korleis dette nettverket av nevron kodar eit mentalt kart er derimot ikkje fullt ut forstått, og det er sparsamt med kunnskap frå eksperiment på menneske. Menneskeforsøk er metodisk og etisk vanskelegare å utføre. I dag er det mest brukte målet på gittercelleaktivitet hos menneske seksdelt rotasjonssymmetri i fMRI BOLD-signal hos menneske som utforsker ei virtuell røynd. Evidensen for at desse signalendringane kjem frå gitterceller baserer seg på elektrofysiologiske opptak av nevron i rotteforsøk, men evidensen er inkonklusiv og har aldri før vore replikert. Replikasjon av dette evidensgrunnlaget kan seie noko om reabiliteten til mykje av forskinga på gitterceller som i dag gjerast med fMRI på menneske. Ved å bruke opptak frå enkeltceller kan ein samstundes svare på delar av eit mykje større spørsmål om dei cellulære mekanismane bak den seksdelte rotasjonssymmetrien ein observerer i fMRI BOLD-signal medan menneske navigerer like så som mekanismen bak fMRI-signalet i seg sjølv.

Introduction

The hippocampal formation

The hippocampal formation is a phylogenetically old structure, highly conserved across mammalian species in regard of both structure and function (*1*). This structure consists of the hippocampus proper with its areas CA1-3, the dentate gyrus (DG), the entorhinal cortex and the subiculum with the adjacent pre- and parasubiculum (Fig. 1). The entorhinal-hippocampal system caught interest early because of their strong reciprocal projections (*2*). Today, the entorhinal cortex is known as a nodal point between the neocortex and upstream sensory cortices on one side, and the hippocampus on the other side (*3-5*). Since the hippocampal projections are reciprocal to that of its input via the entorhinal cortex, the natural idea of hippocampal functioning is modification of the signals it receives.

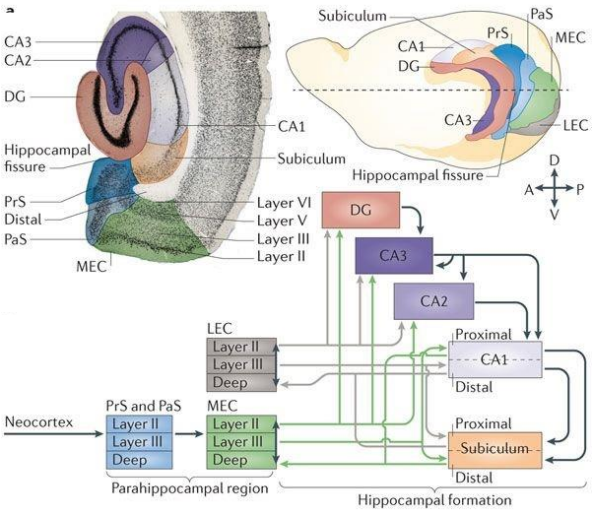

Figure 1| **Anatomy of the hippocampal formation.** Top left shows a transverse section of the hippocampal formation from the right hemisphere of a rat; top right shows a schematic sagittal section (A: anterior, P: posterior, D: dorsal, V: ventral). Together, this shows the anatomical relations between the cornua ammonis (CA1-3), the dentate gyrus (DG), the subiculum, the presubiculum (PrS) and parasubiculum (PaS), the medial entorhinal cortex (MEC) and the lateral entorhinal cortex (LEC). The bottom part of the figure shows the main connectivity between these areas, and emphasizes the entorhinal cortex as a nodal point between the neocortex and the hippocampus.

From: E. I. Moser et al., Grid cells and cortical representation. Nat. Rev. Neurosci. **15**, 466-481 (2014).

A cognitive map of space

Studies of hippocampal functioning in Henry Molaison, also known as patient H.M., who underwent bilateral removal of the hippocampal formation and uncus due to drug treatment-resistant temporal lobe epilepsy, concluded that the hippocampus was crucial both for the formation of episodic memories and spatial navigation (*6, 7*). Investigations of the cellular mechanisms for hippocampal function with single cell electrophysiological recordings in rats lead to the discovery of place cells (*8*). These hippocampal neurons show specific firing at certain locations when an animal freely forages an environment (Fig. 2). Different place cells have different preferred firing locations and could therefore make out a spatial map. The discovery of place cells in the hippocampus lead to the cognitive map the-

ory, proclaiming the hippocampus as a cognitive map of space (*9*). The two functions of the hippocampus – formation of episodic memory and spatial navigation – seem disparate yet should still emerge from the same neural algorithm. Interestingly, it is hypothesised that these two functions emerge from the same mechanism; in other words that navigating in mental space (episodic memory) and physical space (spatial navigation) is based on the same neural encoding (*10*).

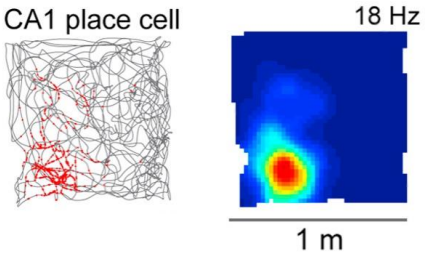

Figure 2 | **Hippocampal place cell.** Electrophysiological single cell recordings from rat CA1 show that some of the neurons have preferred firing to certain locations in the environment. Left part shows the running trajectory (grey) of a rat foraging an open field box (1 m x 1 m), with each spike from this neuron superimposed as red dots coherent to the location of the animal when the spike occurred. Right part shows a heat map of the spiking activity, with red being maximal activity and blue being minimal activity.

From: K. M. Igarashi, The entorhinal map of space. Brain Res. **1637**, 177-187 (2016).

The discovery of place cells led to questions concerning the origin of the space metric. The hippocampus, being far downstream from primary sensory cortices, could either encode the space metric by intrinsic mechanisms, or it could be encoded in another cortical area from which the hippocampus receives input. Due to the minimal intrinsic connections between CA1 cells, which does not hold true for CA3 cells, an intrinsic mechanism would likely be computed by connections between CA1 and CA3 (*11, 12*). However, completely lesioning the CA3 projections to the CA1 proved insufficient to disrupt the sharpness and stability of CA1 place cell firing, thus speaking against an intrinsic mechanism of the hippocampus in the formation of place cells (*13*). Therefore, focus moved towards the parahippocampal region, with special interest of the medial entorhinal cortex (MEC) due to its nodal role between the hippocampus and the neocortex with strong projections to both CA1, CA3 and the DG. Electrophysiological single cell recordings in layer II (LII) and layer III (LIII) of the MEC showed cells with sharp and stable multiple firing fields, similar to those seen in place cells, that even kept their firing properties after lesional removal of the hippocampal output (*14*). Being upstream of hippocampal place cells, and unaffected by removal of hippocampal output, these cells were a likely source for generating place cell activity. These cells were to be known as grid cells (*15*).

Unlike place cells, that has one firing field in a simple environment, grid cells have several firing fields placed in a strikingly regular hexagonal pattern tiling the environment as a mosaic made of solely equilateral triangles. The cells fire irrespective of absence of visual input or changes in the animals speed or direction (*15*). Three distinct features characterize grid cells: scale, phase and orientation. Grid scale describes the distance between two adjacent firing fields; grid phase is the relative

shift of firing fields in the xy-plane; and grid orientation is the angle between the grid axes and the environment (*15*). Grid scale increases along the dorsoventral axis, and grid cells with equal grid scale are more likely to share grid orientation than grid cells with different scale (*16*). This grouping of similar grid cells is called grid modules, and the modular organization goes along the dorsoventral axis of the MEC (Fig. 3). The increase in grid scale is also discretized, increasing with a factor of approximately 1,42 from one module to the next (*17*).

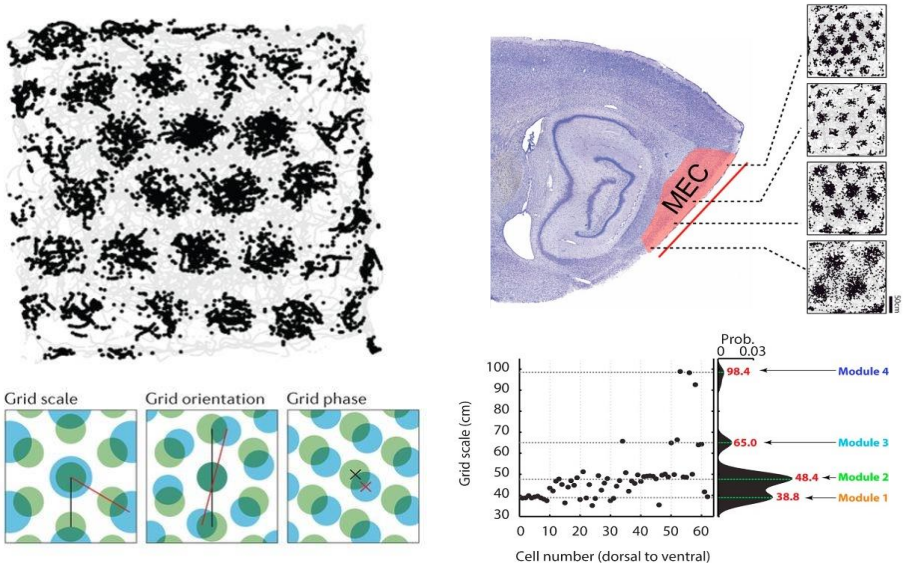

Figure 3 | **Grid cell firing properties and modular organization of grid cells.** Top left shows the firing of a grid cell of a rat foraging a 2,2 m square box in a path plot with running trajectory (grey) and superimposed spikes (black). Note the remarkable hexagonal organization of firing fields. Bottom left shows the three properties in which grid cells variate, scale, orientation and phase, by comparing the firing fields of two simulated grid cells (blue and green). Top right shows a sagittal Nissl stained section from rat MEC (red), with representative plots like top left showing an increase in grid scale along the dorsoventral axis of the MEC. Bottom right shows the discretized organization of grid scale of grid cells from one rat. Cells were plotted successive in the order they were recorded from dorsal to ventral part of the MEC. Cells could then be clustered into discrete modules.

Left panel from: E. I. Moser et al., Grid cells and cortical representation. Nat. Rev. Neurosci. **15**, 466-481 (2014).
Right panel from: K. M. Igarashi, The entorhinal map of space. Brain Res. **1637**, 177-187 (2016).

With the existence of both place and grid cells, the path was set for studying the relationship between these cells. Rooting in anatomical projections, several studies were conducted to understand the independency of these cell types. One such study exploited the different projection from LII and LIII of the MEC to the hippocampus. The superficial MEC projections go to CA1 through either a direct or an indirect pathway. The direct projections go from LIII directly to CA1, whilst the indirect projections go from LII to CA3 and the DG, which successively project back to CA1. Selectively impairing the direct input to CA1 from MEC LIII neurons would therefore lead to altered grid cell input to CA1,

while conserving input to CA3. Such impairment resulted in larger and less sharp firing fields of CA1 place cells, while CA3 place cells were unaffected (*18*). In the reverse direction, studying the entorhinal grid map's dependence of hippocampal input by silencing the hippocampus, grid cells have shown to lose their spatial firing properties when excitatory projects from the hippocampus cease (*19*). Disrupting grid patterns also occur by inactivation of the medial septum and the anterior thalamic nuclei, indicating that a diverse set of input is necessary to form the entorhinal map of space, but also by inactivation of GABAergic parvalbumin+ interneurons in the superficial layers of MEC (*20-23*). Studies in rat pups also show that place cells are detectable and mature earlier than grid cells (*24, 25*). In addition, removal of NMDA glutamate receptors in the MEC selectively disrupt grid cell firing whilst place cells remain their firing fields, but also leads to impaired navigational behaviour in mice (*26*). The neural encoding mechanisms from which these two cell types emerge and cooperate is still not understood, but understanding this would be a major breakthrough in neuroscience as it would describe the cortical representations of space far downstream of any visual or sensory input (*3*).

After the discovery of grid cells, spatial tuning within the entorhinal network was widely investigated. Grid cells were first described in rats, but were later described in mice, bats, macaque and humans (*27-30*). It also became clear that grid cells were a part of a bigger network of other functional cell types in the MEC, as head direction cells, border cells, speed cells and object vector cells were discovered (Fig. 4) (*31-35*). Head direction cells exist in several cortical areas, including the presubiculum, retrosplenial cortex, thalamus and mammillary nuclei, and are cells that fire rapidly when the animal's head is turned in a specific direction (*36-39*). Border cells fire along clear geometric boarders in the environment. Interestingly, both head direction and border cells have mature firing properties in new born rat pups, which could be sufficient for generating place cells in the hippocampus whilst grid cells are still

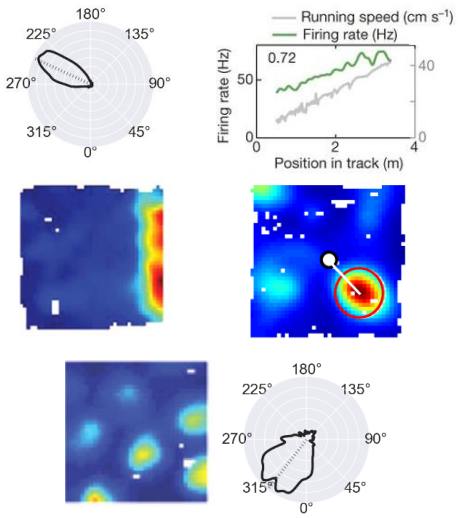

Figure 4 | **Spatial cells of the MEC.** In addition to grid cells, five other spatial cells have been identified in the MEC. These are head direction cells (top left), border cells (middle left), speed cells (top right) and object vector cells (middle left). Many cells exhibit dual functionality, and are so called conjunctive cells. One of the most common dual functionality is conjunctive grid and head directions cells (bottom).

Polar plots: Own data.
Firing rate maps: T. Solstad, C. N. Boccara, E. Kropff, M. B. Moser, E. I. Moser, Representation of geometric borders in the entorhinal cortex. Science **322**, 1865-1868 (2008).
Speed cell: E. Kropff, J. E. Carmichael, M. B. Moser, E. I. Moser, Speed cells in the medial entorhinal cortex. Nature **523**, 419-424 (2015).
Object vector cell: O. A. Hoydal, E. R. Skytoen, S. O. Andersson, M. B. Moser, E. I. Moser, Object-vector coding in the medial entorhinal cortex. Nature **568**, 400-404 (2019).

immature (*40, 41*). Speed cells have a linearly increase in firing rate coherent to running speed, and object vector cells are tuned to both distance and orientation from objects in the environment. In addition, several of the MEC cells have dual functionality. Most striking is the conjunction of head directionality and grid cell firing in cells, often referred to as conjunctive grid cells (*32*). Together, all these functional cell types in the MEC together with the hippocampal spatial cells orchestrate the cognitive map and the ability to navigate.

Studying human grid cell activity

Studying grid cells in primates is challenging compared to studies in rodents, in both methodical and ethical aspects. Electrophysiological recordings in non-human primates is for example challenging due to the ventral migration of the hippocampal formation during evolution, locating it entirely within the temporal lobe, whilst the rodent MEC is located dorsocaudaly, easier accessible for electrophysiological recordings (*42*). In humans, invasive electrophysiological recordings have been possible to perform only in patients with drug-resistant temporal lobe epilepsy, which undergo electrode implantation to locate foci of seizures for possible surgical removal. Implanted patients navigating in a virtual reality (VR) open field environment have shown cells with grid-like firing patterns, suggesting the existence of grid cells in human primates as well as in rodents (*30*). In humans, this approach is little available and has clear constrains to methods that can be utilized. Therefore, functional magnetic resonance imaging (fMRI) based on blood oxygen level dependent (BOLD) contrast has been used combined with VR navigational tasks. For instance, the first indirect measurements pointing towards grid-like activity in humans were obtained using a BOLD fMRI and VR navigational approach (*43*).

BOLD fMRI

In order to understand the basis of grid-like activity in BOLD fMRI, understanding the basics of the BOLD-signal is essential. BOLD fMRI is based on oxygenated and deoxygenated haemoglobin having different magnetic properties. Deoxygenated haemoglobin is paramagnetic, as four out of its six outer electrons are unpaired, while oxygenated haemoglobin is diamagnetic, as all its uncoupled electrons have been coupled with electrons from the bound oxygen (*44*). A paramagnetic substance leads to changes in the inhomogeneity of a magnetic field, resulting in faster T2-relaxation, so that an increase in the concentration of deoxygenated haemoglobin leads to a signal intensity decrease whilst a decrease of deoxygenated haemoglobin leads to a signal intensity increase (Fig. 5) (*45*). In response to increased regional brain activity and higher metabolic needs, neurovascular coupling leads to higher regional blood flood and an increase of local oxygenated haemoglobin (*44*). These changes are detectable with MRI, and therefore BOLD fMRI measures increases in both regional blood flow and volume, in addition to the relative increase of oxygenated haemoglobin in capillaries and venous blood

(*46*). The idealized BOLD-response starts with an initial dip, resulting from an initial increase of oxygen extraction after neuronal activity (*44*). Following, with approximately a 2 seconds delay reaching maximum intensity after 5-6 seconds, comes an increase in local blood flow overshooting the demand resulting in an increased signal intensity, before the signal intensity goes back to baseline (Fig. 5) (*45*). These BOLD changes are not understood at a cellular level, and the order above is only a hypothesized model based around the idea that increased need of oxygen due to oxidative phosphorylation in metabolic active neurons leads to BOLD-signal changes.

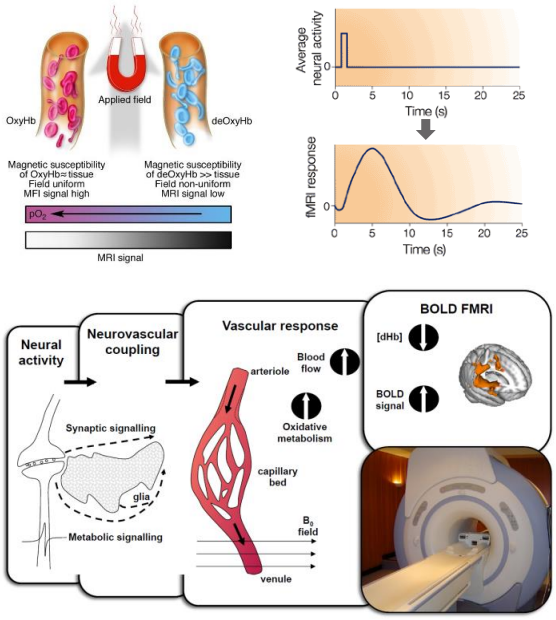

Figure 5 | **Basics of BOLD fMRI.** BOLD fMRI is based on deoxygenated haemoglobin (deOxyHb) having a different effect on the MRI-signal than oxygenated haemoglobin (OxyHb). The BOLD-signal is connected to neural activity by vascular coupling, so that increased neural activity and metabolic need leads to increased local blood flow and increased OxyHb. These changes in perfusion can be detected by changes in especially T2*-weighted sequences, and start with an initial dip of the signal, before reaching a high peak and returning to baseline.

Top left: Gore, J. C. Principles and practice of functional MRI of the human brain. The Journal of Clinical Investigation **112**, 4-9, doi:10.1172/JCI19010 (2003).
Top right: D. J. Heeger, D. Ress, What does fMRI tell us about neuronal activity? Nature Reviews Neuroscience **3**, 142 (2002).
Bottom: Wise, R.. Pharmacological fMRI: Principles and confounds. Cardiff University Brain Research Imaging Centre.

Another hypothesized model concerns the metabolic role of astrocytes. These glial cells base their metabolism on non-oxygen dependent glycolysis, and are highly active shortly after neuronal activity due to their important role in the energy-consuming task of recycling glutamate from the synapses to glutamine (*45*). Therefore, astrocyte activity could lead to higher blood flow because of high glucose demands in astrocytes, secondarily resulting in higher concentrations of oxygenated haemoglobin. Taken together, BOLD fMRI is an indirect measure of brain activity described by complex metabolic and vascular changes.

The wide use of BOLD fMRI has led researchers to address the elusive relationship between fMRI and direct electrophysiological recordings. Simultaneous BOLD fMRI and intracortical electrode recordings in monkey visual cortex has shown a correlation between local field potentials (LFPs) and haemodynamic changes, possibly because LFPs are generated more by internal processing within a cortical area rather than its spiking output (*47, 48*). This indicates that BOLD-signal changes are a result of

internal signalling rather than the spiking output often recording with single unit electrophysiology. However, comparison of invasive electrocorticograpic field potentials (EcoG) and BOLD fMRI in humans have failed to show a correlation in field potentials and haemodynamic response (*49*). A combination of calcium imaging fibre-optics and BOLD fMRI have shown predictable BOLD-signal changes from direct neuronal activity, but also contributions of astrocytic networks to the BOLD-signalling (*50*). Also, a study of mouse haemodynamics showed that changes in the cerebral blood volume was greatly influenced by behaviour, and that at least half of the changes in cerebral blood volume during the resting state was unrelated to cortical processing (*51*). These studies imply that much is still unknown about the correlation between neural activity and BOLD fMRI, making conclusions at the cellular level based on such studies precarious.

The rationale for measuring grid cell activity with BOLD fMRI

As previously mentioned, the first measurements of putative human grid cell activity came from a study measuring the changes in BOLD-signalling in humans navigating in a VR environment (*43*). In this study, human participants were foraging the VR environment using a joy stick to move around while being scanned inside a 3T MRI-scanner (Fig. 6). By investigating the BOLD-signal in voxels (2 mm x 2 mm x 3 mm) of the human parahippocampal region, the researchers discovered that the BOLD-signal increased and decreased periodically. The periodicity corresponded to which direction

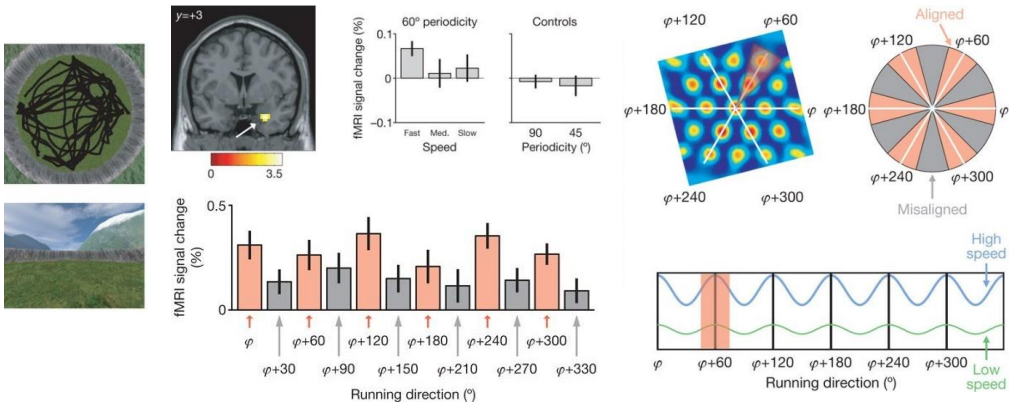

Figure 6 | **BOLD-signal changes are symmetric, six-folded and stronger during fast runs.** Left panel shows the running trajectory (black) of a person exploring the VR-environment during MRI-scanning, and the first person view of the environment that the participants saw. Middle panel shows localized BOLD-signal increase in voxels of the human parahippocampal area. The signal is stronger for runs 60° apart from a baseline (φ), but not for other periods (ex. 45°). The signal is also stronger for fast runs than for slow runs. Right panel shows how a six-fold symmetry of BOLD fMRI ($\varphi + n \cdot 60°$) fits with the axis of grid cells in the MEC. The grid cell autocorrelogram is rotated so that the grid orientation coincides with the baseline φ. Stronger signal for fast runs could then be explained by the animal traversing more grid firing fields, leading to higher grid cell activity, making it measurable with BOLD fMRI.

From: C. F. Doeller, C. Barry, N. Burgess, Evidence for grid cells in a human memory network. Nature **463**, 657-661 (2010).

the participants were moving in the VR environment. Interestingly, the BOLD-signal had increases at increments of 60°, followed by signal decreases in between, resulting in a hexadirectional signal pattern (Fig. 6). This six-fold symmetry could resemble the hexagonal firing pattern showed by grid cells in the MEC. The periodicity was not apparent in controls of 90°, 45°, 72° or 51,4°, corresponding to a 4-fold, 8-fold, 5-fold or 7-fold symmetry. In addition, the BOLD-signal changes were stronger for fast runs than slow runs (Fig. 6). Six-fold symmetry strongly modulated by speed appeared from the entorhinal cortex into the subiculum, as well as in posterior and medial parietal cortex, lateral temporal cortex and medial prefrontal cortex, consistent with the present of either visual, head directional or grid-like coding in these cortices. However, even though the origin of this signal remains elusive, the hexadirectional signal pattern in BOLD fMRI has been used as a measure of grid cell activity (*52-56*).

One possible mechanism behind the hexadirectional BOLD-signal is coherent firing of conjunctive grid cells along the axis of the grid (*43*). If conjunctive grid cells that all share orientation has a preferred firing direction along one of the grid axes, this population would have six preferred firing directions. Even though these cells would have different grid phases, a macroscopic measure as BOLD fMRI could possibly measure increased neuronal activity for runs along these preferred directions. This increased activity would correspond to the recruitment of conjunctive grid cells with the same preferred firing direction, activated at different locations in the environment due to phase differences (Fig. 7). However, the modular organization of grid cells makes this hypothesis troublesome. Even though grid cells of the same module share both grid scale and grid orientation, conjunctive grid cells of different modules would differ in grid orientation. This intermodular orientation difference, however, is more synchronized that what you expect by chance (*57*). For the population of conjunctive grid cells in total, this might lead to a disruption of the six-folded organization of preferred firing directions (Fig. 7) (*17*). In addition, ellipticity of grid cell firing makes this model even harder to fit with the known firing properties of grid cells (*57*). On the other side, this issue can be address experimentally by comparing the grid axis and firing direction of conjunctive grid cells, preferably from many cells and of different modules.

Alignment of grid axis and preferred firing direction of conjunctive grid cells

This experiment is performed in the same article that found the hexadirectional BOLD-signal and that proposed conjunctive grid cells as a candidate for the BOLD-signal changes (*43*). From electrophysiological extracellular tetrode recordings, they provide data from 18 conjunctive grid cells recorded in eight different rats foraging an open field environment for cookies. Analyses on this data show that the preferred firing direction of conjunctive grid cells coincides with one of the grid axis (Fig. 8). Therefore, they argue, conjunctive grid cells could serve as the underlying mechanism of hexadirectional

changes in BOLD-signalling. This finding is, to our knowledge, the only electrophysiological evidence connected to the grid-like activity in BOLD yet has never been reproduced. In addition to analyses of conjunctive grid cells, they show by analysing 113 grid cells recorded from 16 rats that the organization of the grid cells' firing fields were more consistent and regular when the animals were running fast compared to slow. The positive modulation of BOLD fMRI by higher speed could be explained simply by the traversing of more firing fields from more cells in a shorter time, but also by this increased gridness. An obvious weakness in the electrophysiological studies, especially concerning conjunctive grid cells, is the low number of cells. Since this study was conducted, large studies have been conducted to characterize grid cells, leading to datasets with almost tenfold as many cells. In the following, we try to replicate these electrophysiological analyses using the Stensola-dataset. This dataset consists of 968 unique cells recorded with tetrodes from LII-III of MEC in 15 rats, 10 of which were implanted with hyperdrives carrying 12 tetrodes and 5 of which were implanted with microdrives carrying 4 tetrodes. This allows analyses on a vast number of grid cells, and up to 186 grid cells from

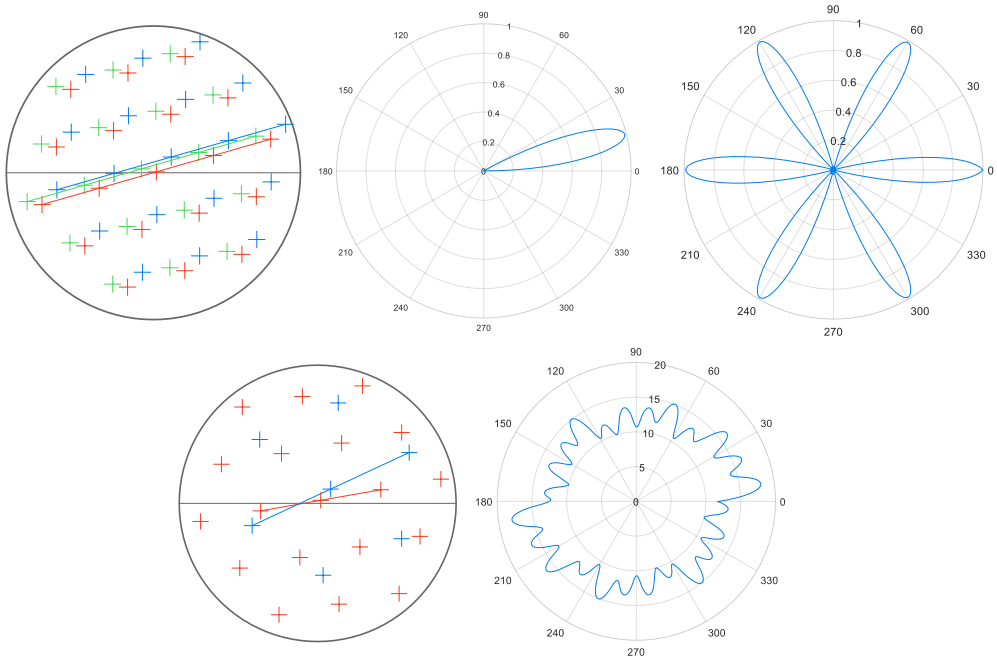

Figure 7 | **Simulation of conjunctive grid cell firing.** Top left shows the firing fields (+) of three conjunctive grid x head direction cells (red, green and blue) of the same module, so that the cells share both orientation and scale. The orientation is marked as a straight line through the firing fields. Top middle shows the preferred firing direction of one of these conjunctive grid cells as a polar plot (head direction as degrees, firing rate as radius), where the preferred firing direction coincides with one of the grid axis. Top right shows a merged polar plot of such a population of conjunctive grid cells of the same module. If all cells fire along one of the grid axes, this would lead to six distinct head directions that would recruit neural activity from this subpopulation of MEC neurons. Bottom left is equal to top left, but shows two conjunctive grid cells (red and blue) of different modules with different scale and orientation. Bottom right shows how a simulated merged polar plot of conjunctive grid cells from four different modules could look. The six-folded symmetry has vanished and the distribution is more uniform.

one animal (*17*). Further, we look for another origin of the hexadirectional BOLD-signal in non-clustered multi-unit activity recorded from the same electrodes.

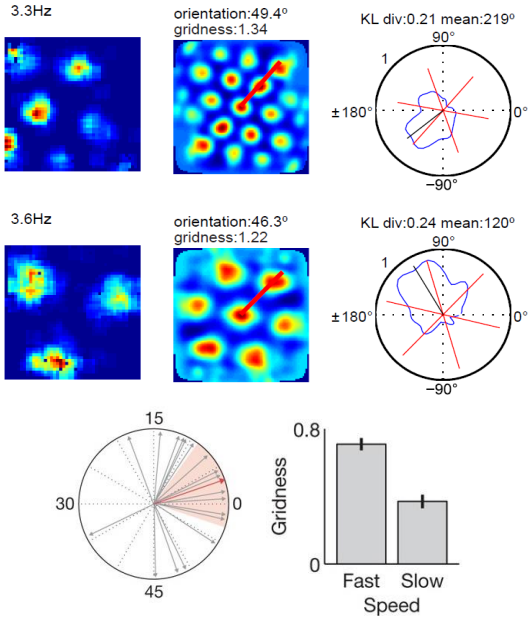

Figure 8 | **The preferred firing direction of conjunctive grid cells coincide with the grid axis.** Top two rows show the firing rate map, the autocorrelation of the rate map and the polar plot of two conjunctive grid cells of different module. Firing rate, orientation, gridness (gridscore, see Results) and head directionality measurements (KL- divergence and angular mean, see Results) are marked above the plots. Orientation is marked as a red line in the autocorrelation maps, and the grid axis are plotted in the polar plots for comparison to the preferred firing direction. Bottom left shows the angular difference between the mean firing direction of each cell (n = 18) and its closest grid axis. This distribution is non-uniform and clustered around 0°, as expected if conjunctive grid cells firing along the axis of the grid. Bottom right shows that the gridness of grid cells (n = 113) is lower for slow runs than fast runs when separated by the median split.

From: C. F. Doeller, C. Barry, N. Burgess, Evidence for grid cells in a human memory network. Nature **463**, 657-661 (2010).

Methods and Results

Classification of grid cells and conjunctive grid cells

In the experimental procedure, rats were freely foraging an open field square environment ranging from 1 m to 2,2 m while looking for cookies. Unit activity was recorded with the tetrodes by amplifying with a factor of 3000-5000 and high-pass filtering from 600-6000 Hz. Spike thresholds were set by the experimenter, around 55 μV. The animal was tracked using two LEDs connected to the head stage and the implant. First, grid cells were defined based on their spatial rate map based on the firing and tracking data. A smoothed rate map was used make an autocorrelation, from which a gridscore was calculated. The gridscore is a calculation of the spatial periodicity of a cell, in brief based on the difference when correlating the original autocorrelation to one turned 60° or 120°, and one turned either 30°, 90° or 150° (for details, see ref. (*17*)). A high grid score indicated a high spatial periodicity of 60°, compatible with the firing of grid cells. Further, grid cells were defined based on a shuffling procedure (for details, see ref. (*17*)). In total, 1044 unique cells recorded from superficial layers of MEC were included in the shuffling procedure. These cells were preselected by eye as cells with grid-like or spatial firing properties. Each of these cells were shuffled for 500 iterations. Only cells exceeding a chance level determined by the 99th percentile of the shuffled distribution, corresponding to a gridscore > 0,444, were classified as grid cells and used in further analyses (n = 882) (Fig. 9). In these cells, grid orientation was defined from the spatial autocorrelation using the six firing fields closest to the central field (“inner ring”). Three axes were defined as the angular distance from a fixed horizontal line (0°)

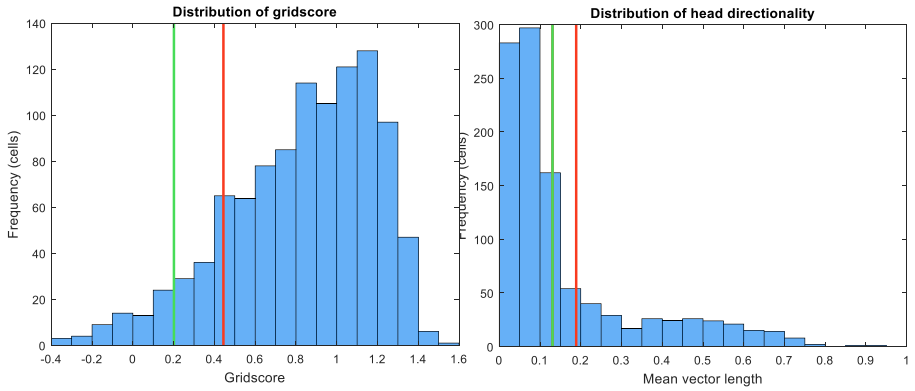

Figure 9 | **Classification of cells based on the shuffling procedure.** Left: Histogram of gridscores in all 1044 putative grid cells. Chance levels described by the 95th and 99th percentile are plotted as respectively green and red vertical lines. 976 cells (93,5 %) exceeded the 95th percentile, and 881 cells (84,4 %) exceeded the 99th percentile. Only cells exceeding the 99th percentile were classified as grid cells. Right: As to the left, but for MVL. 354 cells (33,9 %) exceeded the 95th percentile, and 256 cells (24,5 %) exceeded the 99th percentile. If using the 95th percentile, 321 cells (30,8 %) were classified as conjunctive grid cells. However, only cells exceeded the 99th percentile chance levels for both gridscore and MVL were included, and thus 224 cells (21,5 %) were classified as conjunctive grid cells.

and a line from the central field to three neighbouring fields of the inner ring. As an autocorrelation is symmetric around 180°, the remaining three axes were calculated from these three. Further, grid scale was calculated as the mean distance from the central field to these three fields. For details on all calculations, see (*17*).

Head direction for each position sample in the recording was tracked by the two LEDs on the head stage on the animal. As the head stage is not implanted perfectly along the main axis of the animal, the tracked head direction needs to be corrected. By assuming that the rat usually looks straight ahead when running fast, the head stage offset was calculated as the difference between the head direction and the moving direction of the animal during fast runs. For each animal separately, the mean offsets for all trials were calculated, from which the mean of means were calculated. This value was then used as the head direction offset to correct the tracked head direction in all trials for that animal.
Head directionality can be calculated in several ways, two of which are the Kullback Leibler (KL) divergence and the mean vector length (MVL). Since MVL has been widely used in literature concerning head directionality within the MEC network, we used this as the main method for determining head directionality (*31, 32, 41*). However, since the initial experiment used KL divergence, this was also applied to some extent. Head directionality were, as with grid cells, determined by a similar shuffling procedure of all 1044 cells. Only cells exceeding both the grid cell and head directionality criteria (99^{th} percentile: MVL > 0.189) were characterized as conjunctive grid cells. Of the 881 cells exceeding the grid cell criteria, 224 cells also exceeded the head directionality criteria and were classified as conjunctive grid cells (Fig. 9). Using the 95^{th} percentile of the shuffled distribution, being less strict and possibly increasing the number of false positives, resulted in 976 cells exceeding the grid cell criteria (gridscore > 0.20), of which 321 cells exceed the head directionality criteria (MVL > 0.13) (Fig. 9).

Preferred firing direction of conjunctive grid cells

First, we investigated the relationship between the preferred firing direction and the axis of the grid. For each conjunctive grid cell, we analysed the mean firing direction and found the grid axis nearest to the mean firing direction. The angular firing offset was calculated as the absolute value of the nearest grid axis subtracted from the mean firing direction (Fig. 8). Intuitively, this would lead to a distribution between 0°- 30°, as the maximum angular distance in between two adjacent grid axes is 30°. When looking at all cells from all animals, the mean angular difference between the closest grid axis and the mean firing direction is 15,8° ± 1,2° (mean ± 1,96 sd.). Further, the distribution is uniform and not clustered around 0° (Rayleigh test for uniformity: p = 0,606; V test for uniformity with a known mean, $\mu = 0°$: p = 0,619), unlike the expectation if the mean firing direction was to coincide with the

grid axis (Fig. 10). A few cells showed differences > 30°, which were due to asymmetric or elliptic grid fields.

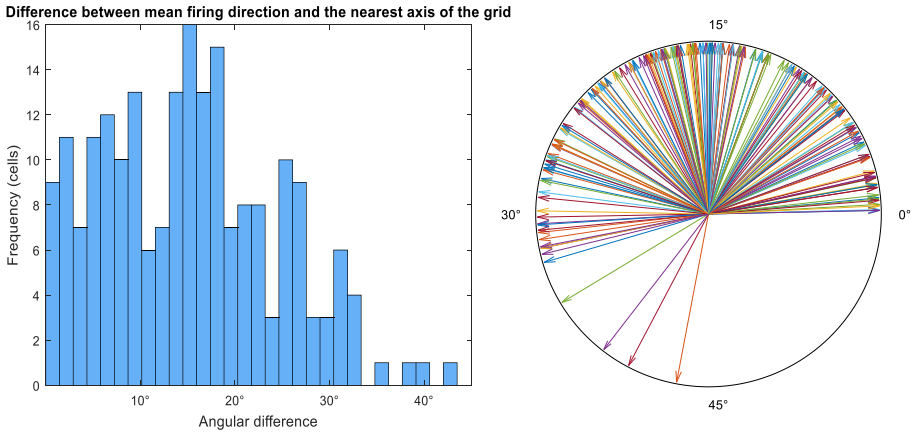

Figure 10 | **Angular difference between mean firing direction and the nearest axis of the grid.** Left: Histogram of absolute angular difference between the mean firing direction and the nearest axis of the grid. The distribution is uniform from 0° and 30° (Rayleigh test: p = 0,606), and not clustered around 0° (V test, μ = 0°: p = 0,619). Right: The same data as in the histogram, shown with arrows (one arrow per cell).

Rat ID	Number of grid cells	Number of conjunctive grid cells	Circular mean (95 % CI)	Rayleigh test	V test
13122	6	1	26,9° (-)	-	-
13261	6	5	14,4° (6,1°-22,8°)	-	-
13468	17	13	21,8° (15,0°-28,6°)	0,008	0,001
13855	103	7	21,6° (10,3°-32,9°)	-	-
13960	71	41	14,7° (11,9°-17,4°)	0,107	0,838
14146	10	4	15,3° (10,5°-20,0°)	-	-
14147	179	47	11,5° (9,0°-13,9°)	0,014	0,489
15314	162	18	21,8° (18,0°-25,0°)	0,260	0,549
15687	13	4	11,7° (2,3°-21,1°)	-	-
15708	101	11	21,3° (17,6°-25,0°)	0,144	0,738
13388	58	18	18,9° (15,2°-22,7°)	0,129	0,689
13473	52	6	12,3° (3,6°-21,0°)	-	-
14257	59	34	15,3° (12,0°-18,6°)	0,555	0,178
14760	12	0	-	-	-
15444	32	16	13,6° (10,0°-17,3°)	0,084	0,981

Table 1 | **Overview of all cells per animal and corresponding circular statistics (see also Fig. 11)** The table summarizes the findings per rat, and shows the number of grid cells, conjunctive grid cells, the circular mean of the difference between mean firing direction and the closes axis of the grid, and circular statistics for rats with at least 10 conjunctive grid cells.

In the original paper, head direction was not measured with MVL but by KL divergence, and a grid cell was classified as conjunctive if tis KL divergence exceeded the somewhat arbitrary value 0,15. We investigated the KL divergency in our population of cells, and found that 148 cells (16,8 %) had a KL divergence > 0,15 (reducing the number of conjunctive grid cells by 28,2 %), indicating that this

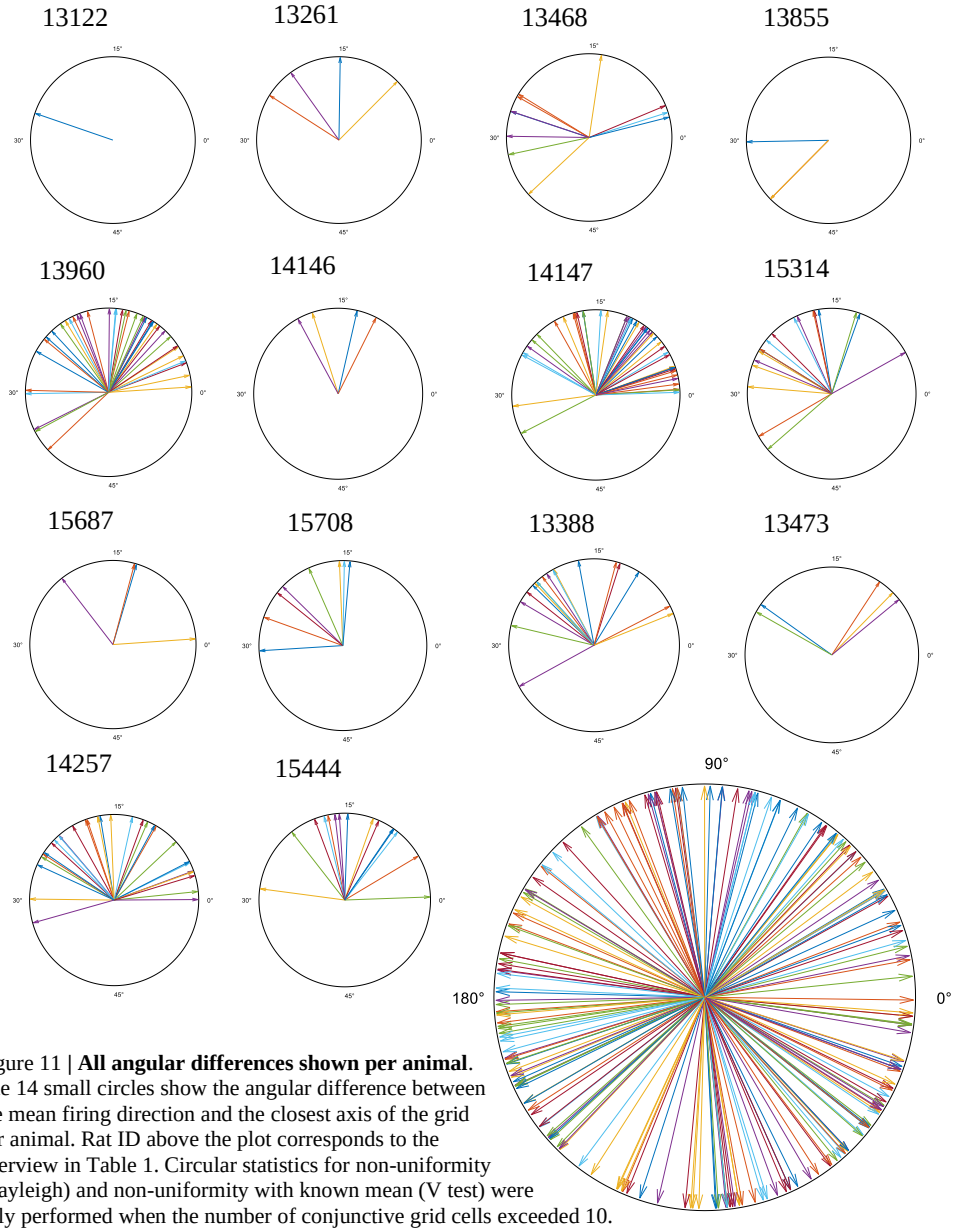

Figure 11 | **All angular differences shown per animal**. The 14 small circles show the angular difference between the mean firing direction and the closest axis of the grid per animal. Rat ID above the plot corresponds to the overview in Table 1. Circular statistics for non-uniformity (Rayleigh) and non-uniformity with known mean (V test) were only performed when the number of conjunctive grid cells exceeded 10. Two rats (13468 and 14147) exceeded chance level ($p < 0,05$) for non-uniformity, of which one rat (13468) also exceeded chance level ($p < 0,05$) for non-uniformity with known mean ($\mu = 0°$). For all other rats, as for all cells together, the distribution was uniform and not clustered around 0°. The big circle shows the distribution of the mean firing direction for all conjunctive grid cells. The distribution if uniform (Rayleigh test: $p = 0,819$).

criterion might be stricter than our 99th percentile of the shuffled MVL distribution. However, this could also mean that the KL divergence criteria is too strict. Next, we re-ran our analyses using the KL divergence criteria for head direction. When looking at the angular difference in all animals, the circular mean was 15,0° ± 1,5° (mean ± 1,96 std.). The distribution was uniform (Rayleigh test: p = 0,38) and not clustered around 0° (V test, μ = 0°: p = 0,382) (Fig. 12). Only five animals had ≥ 10 conjunctive grid cells (13960, 14147, 15314, 14257 and 15444) so that circular statistics were calculated (Table 1). No animal reached the level of significance for either uniformity or clustering around 0°, although one animal (15444) almost reached significance for non-uniformity (Rayleigh test: p = 0,05; V-test, μ = 0°: p = 0,99)

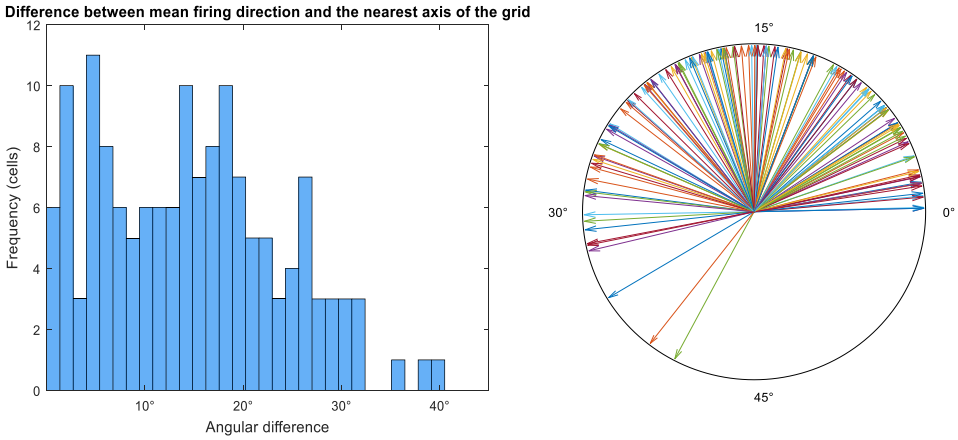

Figure 12 | **Angular difference when KL divergence is used to classify head directionality.** When using KL divergence > 0,15 to classify conjunctive grid cells, 148 cells (16,8 %) were classified as conjunctive. As when using MVL to classify these cells (see Fig. 10), the angular difference between the mean firing direction and the nearest axis of the grid is uniformly distributed (Rayleigh test: p = 0,38) and not clustered around 0°.

As grid modules tend to act independently, we next asked if this was the case for conjunctive grid cells of different modules as well. To classify all grid cells into modules, we used grid spacing as it is the most prominent feature that separates modules (Fig. 13). As previously described (*17*), the number of modules per animal was determined by the number of peaks, *k*, in a kernel density plot of the logarithmic grid spacing. Modular identity of cells was then determined by k-means clustering for *k* clusters, as the best fit after 300 iteration per rat. All grid cells per animal were used for these analyses, and in consistency with

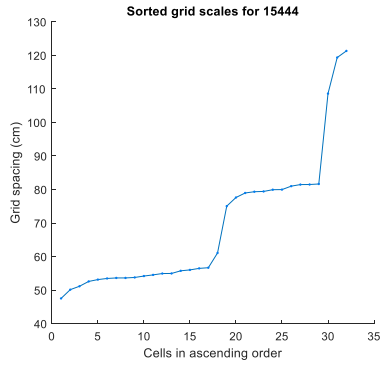

Figure 13 | **Grid spacing as a prominent feature of grid modules.** This plot shows the distribution of grid spacings for all cells in rat 15444 when sorted in ascending order. Note the stepwise increase in grid spacing, consistent with the three modules in this rat.

the original paper of this dataset, this revealed up to four discretized modules per rat.

Next, we analysed conjunctive grid cells from the same module per rat. As this is a great down sampling of our data, only few rats gave enough cells to apply circular statistics on their distribution. Only cells from modules with more than two grid cells were analysed, while modules of two or fewer cells were considered as outliers that might not share similar functional features. Only five rats (13960, 15314, 15708, 1338 and 14147) had enough cells to perform statistical test on at least one of the modules. For most cases, the distribution of angular differences were uniformly distributed and not clustered around 0°. For one animal, the distribution of module 2 reach level of significance for non-uniformity, but the distribution was not clustered around 0° (Fig 14).

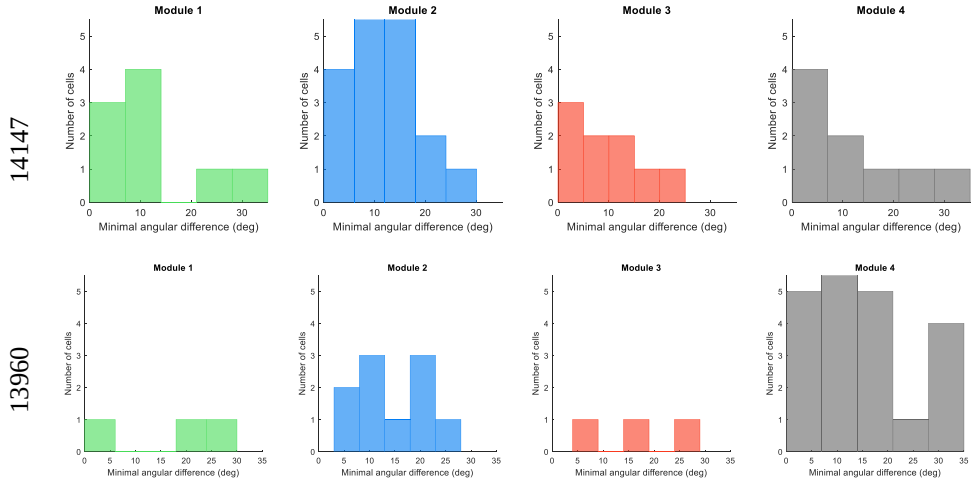

Figure 14 | **Angular differences are uniform across modules.** Top: All angular differences between mean firing direction and the closest axis of the grid for the conjunctive grid cells of rat 14147. This rat has four different modules, and the angular difference is shown for the cells of each module separately. The distributions were uniform for all modules (Rayleigh test: $p > 0,05$) except module 3 (Rayleigh test: $p = 0,03$). For all modules, the distributions were not clustered around 0° (V test for uniformity with a known mean, $\mu = 0°$: $p > 0,05$). Note that in this animal only module 2 exceeded a total of ten cells ($n = 20$), all others had nine cells, making these statistical tests for circular uniformity less applicable. Bottom: Same as top, but for rat 13960. Only module 2 and 4 exceeded ten cells (module 2: $n = 10$; module 4: $n = 25$). For module 4 the distribution was not uniform (Rayleigh test: $p = 0,03$), but was not clustered around 0° (V test for uniformity with a known mean, $\mu = 0°$: $p = 0,72$).

Effect of running speed on gridscore

As introduced earlier, an increase in hexagonality in fMRI BOLD-signal during fast runs compared to slow runs was hypothesized to origin from more grid cell firing fields traversed and thus activation of a greater population of grid cells. Therefore, we also try to replicate the finding that gridscore increases when looking at spikes from fast runs compared to slow runs. To do this, all cells classified as grid cells with at least 1500 spikes were used. All spikes were divided into three groups of equal size

based on running speed, and then gridscore was calculated for three categories of running speed: low, medium and high. In total, 732 grid cells were analysed. The mean grid score for all these cells was 0,95 (95 % CI: 0,93-0,96), and dropped significantly for high 0,71 (0,68-0,73) and medium speed 0,72 (0,69-0,74), and again for low speed 0,46 (0,43-0,49) (Fig. 15). By first look the distributions appeared normally distributed, however, upon testing this appeared not to be the case (one-sample Kolmogorov-Smirnov test: $p << 0,01$ for all groups; Lilliefors test: $p << 0,01$ for all groups). Therefore, after distribution fitting, non-parametric tests were applied to check for statistical significance of the medians. The difference of medians was significant between all spikes and high speed (Wilcoxon rank sum: $p << 0,01$); between all spikes and medium speed (Wilcoxon rank sum: $p << 0,01$); and between all spikes and low speed (Wilcoxon rank sum: $p << 0,01$). When comparing the different speed bins to

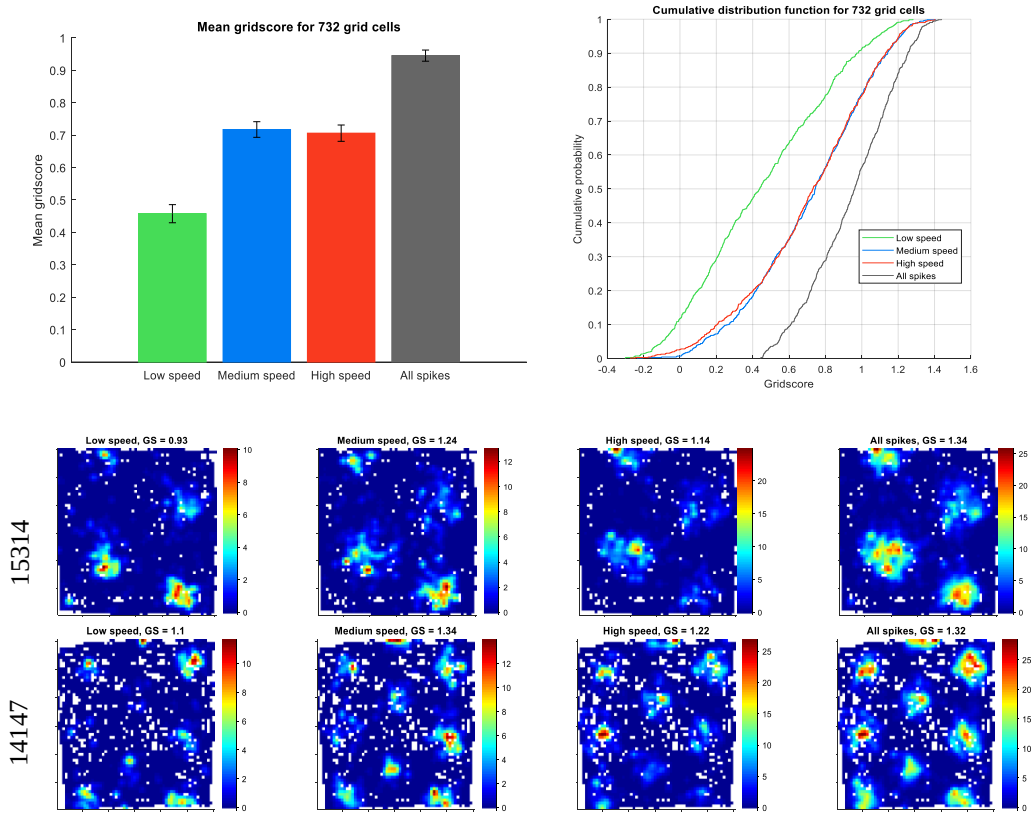

Figure 15 | **Gridscore increases with running speed.** Top: Left plot shows the distribution of mean gridscore for all grid cells with at least 1500 spikes. Spikes are sorted into three equally sized groups: low, medium and high speed. Mean gridscore with 95 % confidence interval is shown. Grid score increases significantly as running speed increases, but only from slow runs to medium runs. In addition, gridscore rises significantly when using all spikes. Right plot shows the cumulative distribution function of the same data. The same effect is noticeable, with lower gridscore from spikes during slow locomotion than for fast. Bottom: Rate map from two example grid cells from rat 15314 (top row) and 14147 (lower row), colorbar showing firing rate (Hz). These cells have at least 3000 spikes and show an increase in grid score with faster running speed. Again, highest gridscore it calculated from all spikes.

each other, the difference of median between fast speed and slow speed was significant (Wilcoxon sign rank test: $p << 0,01$); which also held true between medium and slow speed (Wilcoxon sign rank test: $p << 0,01$). The medians between medium and fast speed, however, did not differ significantly (Wilcoxon sign rank test: $p = 0,36$). This difference is also visible in the cumulative probability function of these four distributions and when looking at the raw rate maps of grid cells (Fig. 15). This might suggest that grid cells have stronger spatial tuning during fast locomotion, or rather that spatial tuning is weaker when the animal barely moves and is more prone to errors. Given the seemingly importance of running speed, input from speed cells might work by correcting the internal path integrator, like the sharpness of grid cell firing.

Multi-unit activity from MEC tetrodes

After having looked at the activity of single units, we next explored whether we could uncover a periodic modulation in electrophysiological data corresponding to the macroscopic changes in fMRI BOLD by looking at multi-unit activity (MUA). To do this, we looked at all spikes recorded from all 12 tetrodes in the 10 hyperdrive rats for 229 sessions corresponding to the sessions from the single cell analyses without doing any clustering. Due to the high-pass filtering from 600-6000 Hz during unit recording, our MUA therefore consists of activity from several cells, but removed background noise recorded by the system as low frequency bandwidths were filtered out. The MUA of these 12 tetrodes may resemble the brain activity from a voxel as measured in fMRI better than activity with single cell resolution, and thus may reveal a periodic firing alike that described in fMRI. Since the changes in BOLD-signal are described to be stronger for fast movement, we also separated the MUA by running speed and looked for periodic changes in firing rate.

From each session, we first extracted the MUA firing rate per tetrode and calculated its tuning curve, before summing the 12 tetrode tuning curves up to calculate the trial tuning curve. Trial tuning curves, which are histograms of firing rate over 360°, were normalized for firing rates to range between 0-1 for comparison across trials. The same procedure was performed for MUA at high running speed. To determine what high running speed could be defined as, we looked at the distribution of all speeds. When comparing the running speeds for all recorded timestamps to the running speed at spiking (Fig. 16), spiking is slightly correlated with higher running speed and the median between the two distributions is significantly different (speed at all timestamps: median 13,8 cm/s; speed when spiking: median 15,1 cm/s; Wilcoxon rank sum: $p << 0,01$). Although the difference is statistically significant, it is arguably different for the behaviour of the rats. Many thresholds were tried, and we ended up using 30 cm/s as a lower threshold for high running speed. This coincides fairly with the 85^{th} percentile of speeds for all movement and for movement when spiking and should be a reasonably high threshold that still allows enough data for further analyses (Fig. 16).

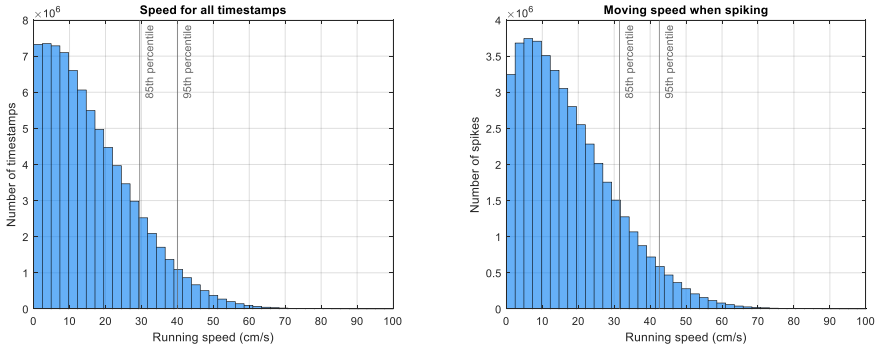

Figure 16 | **Distribution of running speed and filtering of spikes.** Left: Histogram of the running speed for all recorded timestamps, for all trials across animals. The distribution is half-normal (median: 13,8, 25th percentile 6,6 and 75th percentile 23,6. The 85th percentile at 29,5 cm/s and the 95th percentile of 40,0 cm/s are denoted by grey lines. Both these values, and others, were tested for a threshold for filtering out spikes with fast running speed, but both resulted in few spikes and little data to analyse further. Right: Histogram of the running speed when spiking. The distribution is slightly skewed to the right compared with the running speed at all timestamps (median: 15,1, 25th percentile 7,5; 75th percentile 25,3). The 85th percentile at 31,5 cm/s and the 95th percentile of 42,6 cm/s are denoted by grey lines. The two distributions differ significantly (Wilcoxon rank sum: $p << 0,01$).

For all spikes, the MUA tuning curves appeared uniform with no clear periodicity (Fig. 17), which also held true upon statistical testing of circular uniformity (Rayleigh test: $p > 0,70$ for all trials tested separately). The high speed MUA tuning curves were less homogeneous (Fig. 17), but most still looked uniform. Upon statistical testing this also appeared to be the case, were 5/229 trials were significantly non-uniform (Rayleigh test: $p > 0.05$ for 224/229) and the distribution of p-values covered more or less the entire interval between 0-1 (Fig. 17). Of the 5/229 non-uniform tuning curves, two came from rat 13261, one from rat 13468 and one from rat 14147 (Fig. 17). The tuning curves from these trials show a peak at 180° for two of the rats, one peaking at 30°, and all seem to have stronger tuning from 300° and upwards. However, no clear periodic firing emerges and many have very low tuning. Further, the three trials without stronger tuning at 180° have somewhat few speed filtered spikes (< 3500) compared to many other trials (> 10 000).

To further investigate periodicity in this signal, we first performed a Fourier transform of the MUA tuning curves to unravel any periodic firing. By performing the Fourier transform, we could split the signal into a series of sine waves described by their periodicity and amplitude given by the xy-coordinates of the peaks in the frequency spectrum of the transform. No peak threshold was set, and all local peaks in the frequency spectrum were extracted. As expected, the Fourier transform showed little periodicity when performed on all MUA tuning curves. This is seen by a clustering of low-amplitude, low-periodic peaks in the frequency spectrum resembling small harmonic deviations from a constant line (Fig. 18). When performing the transform on the speed filtered MUA tuning curves, this also showed a

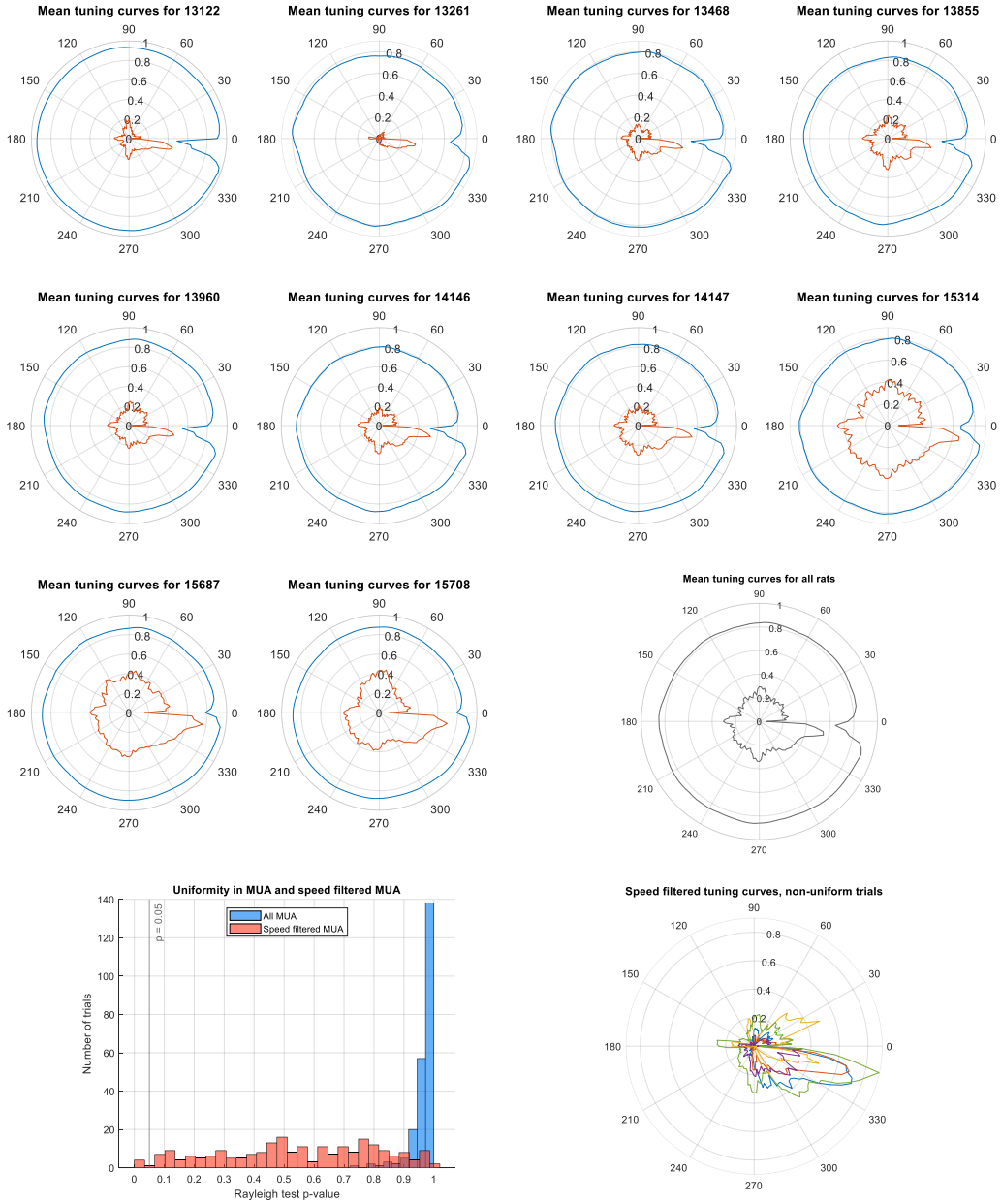

Figure 17 | **MUA tuning curves and speed filtered MUA tuning curves are uniform.** Top three rows: These polarplots show the normalized firing rate per moving direction for each rat, plotted as the mean of the angular tuning curves for all trials in that rat, both for all MUA (blue) and speed filtered MUA (red). All rats have uniform all MUA tuning curves, while the speed filtered are less homogenous, but still mostly uniform. Middle right: Plot as for each rat separately, but here as the mean over all rats. The tuning curves are uniform and show no clear pattern in periodicity (Rayleigh test for circular uniformity: p = 0,99 for all MUA; p = 0,43 for speed filtered MUA). Bottom left: Distribution of p-values from the Rayleigh test for circular uniformity. The speed filtered tuning curves are less uniform than for all MUA, but only 5 trials reach significance at p < 0,05. Bottom right: Speed filtered tuning curves with significant non-uniformity. All five tuning curves show a bigger tendency towards directions greater than approximately 300°.

cluster of low- amplitude low-periodic peaks, but also a greater variety in the frequency spectrum with both longer periods and more prominent amplitudes. For instance, the median amplitude for all MUA was 0,011, while the median for speed filtered MUA was 0,028. Interestingly, when we looked at the 5 % peaks with highest amplitude, a top at both low-periods and at 120° emerged, but none at 60° (Fig. 18). There were some tendencies towards greater amplitudes for periods of both 45°, 50°, 90°, 120°,

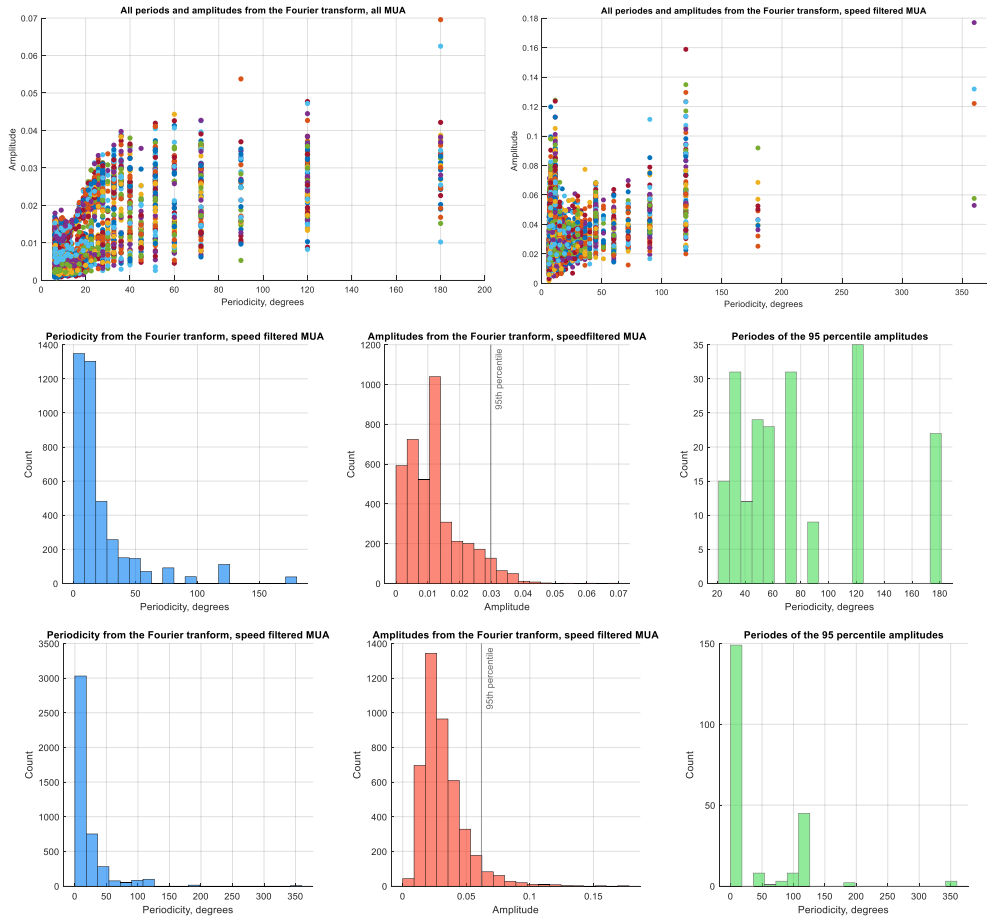

Figure 18 | **Periods and amplitudes from the Fourier transform.** Top: Scatterplots showing the relationship between period and amplitude from all 229 trials when looking at all MUA (left) and speed filtered MUA (right). The plots – especially for all MUA – reveal clustering of low amplitude and low periodic peaks, but also some clustering around both 10°, 40°, 45°, 50°, 60°, 72°, 90°, 120°, 180° and 360°. Middle: Histograms showing the periods (blue) and amplitudes (red) from performing the Fourier transform on all MUA. The results are skewed to low periods and low amplitudes. The most prominent peaks, defined as peaks with amplitudes above the 95th percentile of all amplitudes, are displayed separately (green) and show higher amplitudes for periodicity of both 30°, 60°, 90°, 120° and 180°. Bottom: As middle pannel, but from performing the Fourier transform on speed filtered MUA. There are in total many more peaks in the frequency spectrum, resulting in more period-amplitude pairs. Also, they have higher amplitudes. Still, there is a lot of low-frequency periods, but plotting the 5 % pairs with highest amplitude (green) also reveal a clustering around 45° and 120° periods, without much contribution from a 60° periodicity.

180° and 360°. The clustering at equal periods for the longer periods is likely due to few datapoints feed into the transform (360° binned at 3°, resulting in 120 datapoints per trial).

Secondly, we looked for periodic firing by calculating the autocovariance of the trial tuning curves for both all MUA and speed filtered MUA. The autocovariance was calculated by subtracting the mean of the trial tuning curve from each datapoint in the trial tuning curve, and then autocorrelate it. Periodic firing could be unravelled by peaks in the autocovariance. To specifically look for periodicity of 60°, we calculated an autocovariance score defined by the ratio between the summed autocovariance values at 60° and 120°, and the sum of the autocovariance values at 30° and 90°. A high score would indicate a harmonious pattern in the firing rate with 60° periods, a score around 1 would indicate no such periodicity, and scores <1 would indicate firing anticorrelated to 60° periodicity.

$$Autocovariance\ Score\ = \frac{Autocovariance\ (60°) + Autocovariance\ (120°)}{Autocovariance\ (30°) + Autocovariance\ (90°)}$$

The autocovariance and the corresponding score was calculated for all trials. Most trials showed very low autocovariance, and no harmonic changes (Fig. 19). As for the Fourier analyses, stronger autocovariance was shown at peaks with several periods and with several strengths. When looking at all 229 autocovariances one by one for all MUA, no clear patters emerged, and when averaging over all trials the mean showed no strong tendencies (Fig. 19). However, when looking at the autocovariance of speed filtered MUA, a periodic pattern of 10°-12° as well as 45° was clear, and quite strong in rats with many trials. The value of autocovariance is small, but periodic for 10°-12° shifts, while it is stronger with peaks > 0,5 for 45° shifts.

When plotting a histogram of all autocovariance scores, it showed a small right-sided tail for all MUA and mainly values < 1 for speed filtered MUA (Fig. 20). We took a closer look at trials with an autocovariance score > 2,0 and saw little resemblance of 60° periodic firing (Fig. 20). The max score at 10,9, for instance, was mainly driven by a very low denominator and almost no true increased autocovariance at 60° and 120°. Quite strikingly, the speed filtered MUA showed strong anticorrelated 60° firing judged by the autocovariance score.

Taken together, the Fourier analyses and the autocovariance analyses pointed towards periodicity in tuning curves at periods of 10°-12°, 45° and 120°, but not so at 60°. Therefore, we reran our analyses to test for firing at these periods. We redefined our autocovariance score, and looked first for correlated firing at 45°, 90° and 135° together with anticorrelated firing at 24°, 66° and 111°. For speed filtered MUA, this resulted in 27 trials reaching an autocovariance score > 2, and 92 trials reached a

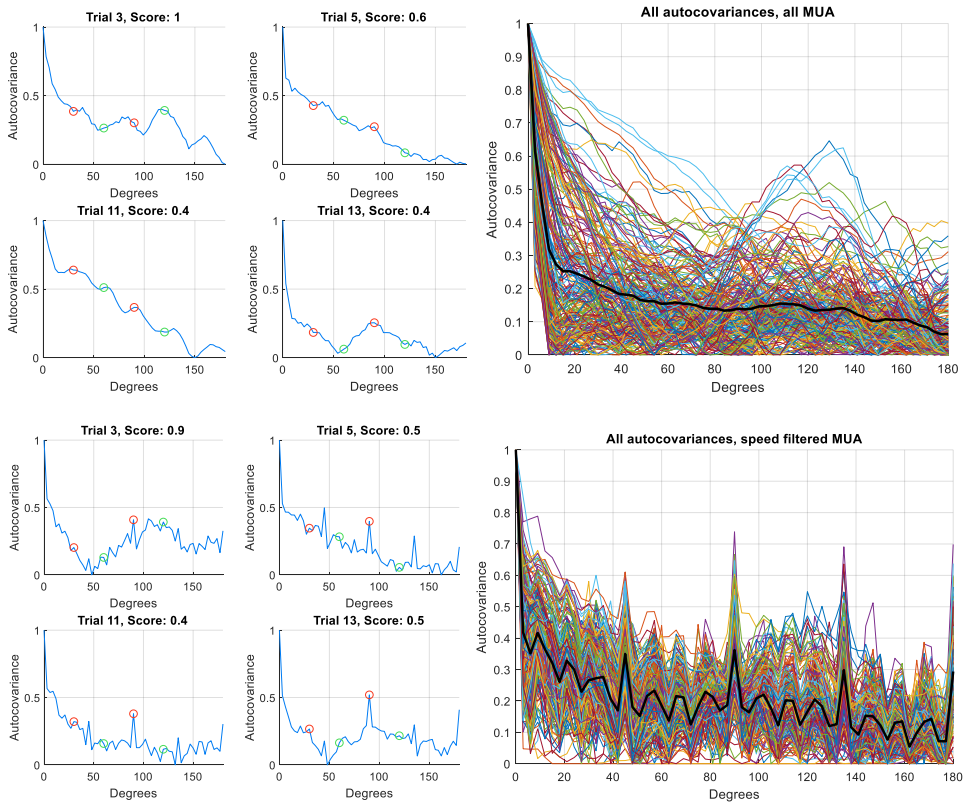

Figure 19 | **Autocovariance curves and scores.** Top left: Example of autocovariance from rat 15687, four trials with the autocovariance for all MUA (blue) and autocovariance score denoted in the title. Circles indicate firing at 60° and 120°, whilst red circles indicate firing at 30° and 90°. Top right: When plotting all autocovariance curves for all 229 trials, no strong modulation appears in all MUA, and the mean signal (black) is mostly flat. Bottom left: Example of autocovariance from the same trials as above, but for speed filtered MUA. Green and red circles as above. None of these four trials show any 60° periodicity. Bottom right: All autocovariances for speed filtered MUA, as in the plot above are the mean of all plotted in black. Unlike the results from all MUA, this reveals periodic firing with approximately 10-12° periodicity and a stronger tuning with 45° periodicity.

score > 1,5 (Fig. 21). By using a score to fit 120° periodicity (autocovariance at 120° times two, divided by the autocovariance at 60° + 180°) for the speed filtered MUA, 13 trials reached a score > 2,0 and 24 trials reached a score > 1,5. Next, we tested the contribution of 15° periodicity by looking for correlation at 15°, 30°, 60° and 75° against anticorrelation of 21°, 36°, 66° and 81°, avoiding multiples of 45°, by which only three trials reached a score > 1,5, were two of them also reached a score > 2. Lastly, we wanted to test for 10° and 12° periodicity. With a binning of 3°, however, the shift between correlated and anticorrelated runs becomes narrow. Nevertheless, we calculated a score in similar fashion as before, using the sum of autocovariance values from 12°, 24° and 36° against 18°, 30° and 42° to test for 12° periodicity. This resulted in 76 trials reaching a score > 1,5, of which 21 trials

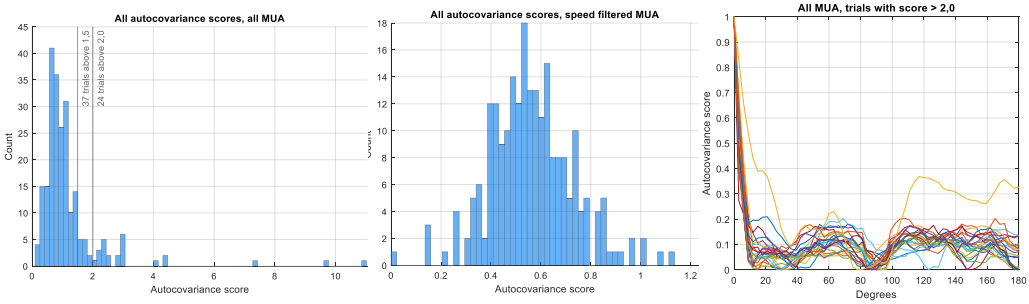

Figure 20 | **Distribution of autocovariance scores.** Left: Autocovariance scores when looking at all MUA tuning curves. The plot shows a right-sided tail, and the distribution does not differ from a random distribution with median 1 (Wilcoxon sign rank test: p = 0,25). 16,2 % (37/229) of the trials have a score > 1,5, while 10,5 % (24/229) of the trails have a score >2,0. Middle: Autocovariance scores from the speed filtered MUA tuning curve show no tail, have mainly values < 1 and differs from a random distribution with median 1 (one sample t-test: p <<< 0,001). No score were above 1,5, with maximal autocovariance score of 1,13. Right: The 24 trials with autocovariance score > 2 show no strong autocovariance at 60° or 120°, but rather quite low values at 30° and 90°.

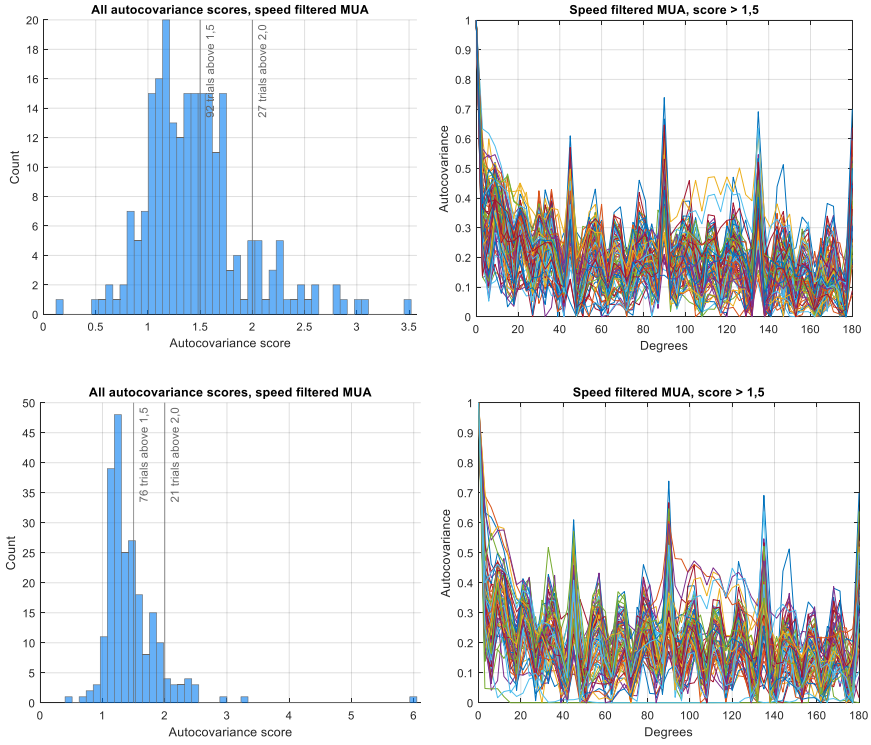

Figure 21 | **Autocovariance curves with autocovariance score for 45° and 12° periodicity.** Top: Distribution of all autocovariance scores from all speed filtered MUA trials when testing for 45° periodicity. The distribution show tendencies towards values > 1, and 92 trials have a score >1,5. These autocovariances are plotted to the right, showing clear peaks at 45°, 90° and 135°. Bottom: As above, but when testing for 12° periodicity. The distribution show strong tendencies to values > 1, and 76 trials have an autocovariance score > 1,5. These trials are plotted to the right. Stronger peaks at 45° periodicity is also clear in these trials and are notably higher than peaks at other multiples of 12°.

also reached a score > 2,0. From the tuning curves with high scores, it was also apparent that these trials overlap with trials showing 45° periodicity, and vice versa, and 55 % (42/76) of the trials also has a score >1,5 when testing for 45° periodicity (Fig. 21). When testing for 10° periodicity we calculated the score by autocovariance at 9°, 21° and 30° against anticorrelated values of 15°, 24° and 36°. Here only 10 trials reached a score > 1,5, were two also reached a score > 2, which was strikingly different from 12° periodicity.

As a final analysis, we compared the results from the Fourier transform of speed filtered MUA in trails with an autocovariance score >1,5 when looking for 45° periodicity. This showed, again, a clustering of low-amplitude low-periodicity peaks in the frequency spectrum, but also showed high amplitude peaks at periods of 10-12° and 120° (Fig. 22). As expected, we also saw a clustering of periods of 45° and 90° (Fig. 22). Taken together, this shows that there are many harmonic elements needed to describe the variations in speed filtered MUA tuning curves, and that the Fourier transform can separate our tuning curves into many smaller elements especially for lower periods, whilst the autocovariance and the autocovariance scores are tools applicable to look for specific periodicity, even for higher periods.

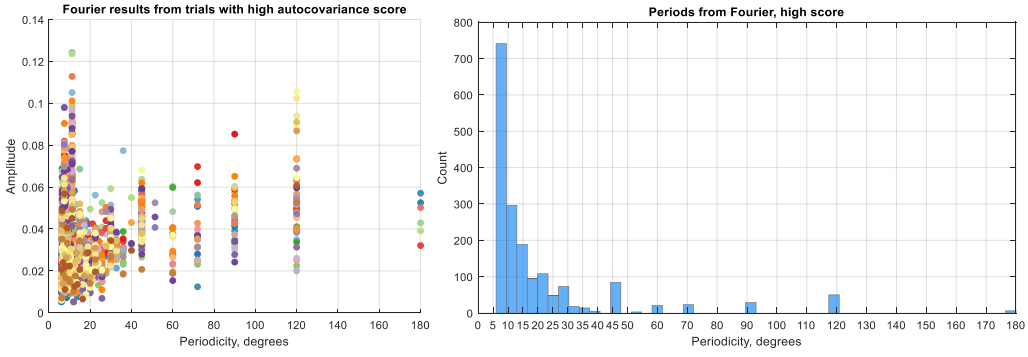

Figure 22 | **Comparison of the Fourier transform and autocovariance.** Left: Scatter plot of period and amplitude pairs from the frequency spectrum of the Fourier transform, from trials of speed filtered MUA with high autocovariance score when looking for 45° periodicity. The scatter shows that periods associated with high periods are similar to the earlier Fourier-analysis and the autocovariances, with peaks around 10°-12°, 45°, 60°, 75°, 90° and 120°. Different colour indicate different trials. Right: Histogram of all periods from the same trials as to the left. The histogram shows the strong clustering at low periods, but also a prominent peak at 45° together with smaller peaks at 60°, 70°, 90° and 120°. This shows that the periodicity of 45° is clear across methods, and that the Fourier transform can separate tuning curves into more than one harmonic component.

Conclusion

A major pillar of science is reproducibility of experiments; that others can get similar results when performing the same experiment that someone else has reported. In the strive for further knowledge and deeper understanding, novel findings are pursued and published in high impact papers whilst reproduced results that either strengthen or weaken the claims of previous studies usually get far less attention. The primary goal of this work was to replicate previous findings that suggested a mechanism for 6-fold symmetry in BOLD-signalling. This was especially interesting since the original results were based on a small data sample, and that the claims from these results has been used in later research without it ever being reproduced. Further, we looked for other possible explanations for a mechanism behind the 6-fold symmetry in electrophysiological data from rats.

First, we analysed a far greater number of conjunctive grid cells from MEC LII-III (n = 224) and found that the preferred firing direction of these cells does not coincide with one of the six grid axes. The distribution of firing directions were uniform around the grid axes, and the angular proximity of the preferred firing direction and the closest axis did not cluster around 0°. This opposed the previous finding, were conjunctive grid cells were indeed showed to fire along one of the grid axes. This claim, however, is based on few cells (n = 18) recorded from 8 different rats. Another weakness in the original finding is that grid axes are defined with perfect 60° firing, where two of the axes are calculated from the first by integers of 60°. In our analyses, we used the true axes of the grid by calculating the angle for all three fields in an auto-correlogram. This would for instance take ellipsoid grid cells into account and does not bias our finding towards periodicity of 60°. In addition, 6-fold symmetry in BOLD fMRI caused by conjunctive grid cells firing along the grid axes is hard to explain when accounting for grid phase and orientation, especially across modules.

Since we had enough cells in our dataset, we also looked at subdivisions of conjunctive grid cells by looking at grid modules separately. Since grid modules have been shown to act somewhat independently of each other, it could be the case that some cells show alignment of grid axes and preferred firing direction. However, this appeared not to be the case. The difference in firing direction and grid axes were just as uniform when looking at modules one by one, suggesting that this is not a mechanism or feature of conjunctive grid cell firing for neither all nor subdivisions of these dual-typed cells.

Interestingly, BOLD fMRI signal changes are stronger during fast runs compared to slower runs. When we tested how running score affect the gridness of all analysed grid cells, we did indeed find stronger gridness for faster runs. Or rather, it seems like slow runs are associated with less stringent grid cell firing. Notably, gridness is most stringent in grid cells when regarding all spikes rather than

separating them into equally sized groups based on running speed. This feature could be a result from down sampling, since grid score is easily influenced by few spikes. On that aspect, one could expect that the scores where equal for slow and fast runs since the number of spikes were equal for each group per cell. In addition, the score is also affected strongly by coverage, and lower moving speed would indicate less coverage. This could affect the results so that true grid cells only get to fire in one firing field due to little movement and would therefore get a bad grid score, while spikes for greater moving speed would get more coverage and visit more firing fields, so thus result in a higher grid score. If grid cells fire more stringently during fast runs holds to be true, this might imply that the MEC speed cells are important for updating the cognitive map, and that these cells are more actively correcting other functional MEC cells when movement is increased.

By our findings, the 6-fold symmetry seen in BOLD fMRI in humans navigation in VR can not be ascribed to conjunctive grid cell firing. Therefore, we asked if other aspects of electrophysiological data than single cell recording could explain it. By looking at all MUA from recording trials within the MEC of rats, we were unable to distinguish any periodic firing patters in the angular tuning curves for any of the 229 trials. The MUA is, however, a crude measure that includes both true cell activity and noise recorded by the recording system when the animal for instance grooms or eats. A periodic pattern could therefore drown in an enormous amount of noise and overall activity.

Since the BOLD-signalling is shown stronger for fast runs, we did the same analyses on speed filtered MUA and wanted to see if this could help in unravelling periodic firing patterns. When filtering out approximately the 15 % of spikes with highest running speed, we discovered a pattern of periodic firing both at single trials, across trials and across rats. The periodicity, however, did not match a 6-fold symmetry with 60° periods, but rather an 8-fold symmetry at 45° periods and a weaker 30-fold symmetry at 12° periods. Also, periods of 120° suggesting 3-fold symmetry was apparent in several trials. Nevertheless, when looking at autocovariance of the angular tuning curves, 45° periodicity was clearly the strongest component of angular tuning for speed filtered MUA. Such a periodicity has shown no correlation with changes in BOLD-signalling. The effect was not apparent when we analysed all MUA, which might indicate that the contribution to this firing pattern is weak compared to all firing. Also, a strong component at 45° could have undermined our tests for 60° periodicity. When testing for 60° periodicity, we expected anticorrelation at 90°. Since many runs had strong 45° periodicity, our seemingly missing finding of 60° periodicity could rather be a result of high correlation at 90°, as expected by strong 45° periodicity. Yet, this would imply that a 45° periodicity is stronger than a 60° periodicity and should therefore have been more prominent in fMRI BOLD if this finding is applicable to BOLD. Since our data consisted of cells from both LII and LII of MEC, it could also be the case that the two layers differ in periodic tuning, and could make a true tuning hard to unravel.

Just as it is hard to draw conclusions at cell and population level from fMRI BOLD is it also hard to hypothesis on how BOLD-signalling would be affected based on findings from electrophysiological MUA. As our first finding imply, one should be wary of concluding upon cellular mechanisms on small samples, and especially when extrapolating mechanisms from single cell recording to macroscopic indirect measures such as fMRI BOLD.

That 45° periodicity stick out was puzzling and not expected. One possible explanation could for instance be that it occurs as a result of the rats foraging square environments. Testing for the same periodic tuning in data from rats running in circular boxes would therefore have been interesting. Sadly, all of the rats in this dataset were tested in square environments. Further, it would be interesting to see if there are correlations between EEG and fMRI. Both methods are indirect and population based measures of brain activity, and might therefore be more comparable to each other than to electrophysiological single cell recordings and MUA. Since EEG-data often are available through tetrode recordings and that EEG oscillations within the entorhinal-hippocampal circuit is thoroughly studied, such experiments might give insight into what the 6-fold symmetry fMRI BOLD-signal originates from.

References

1. J. R. Manns, H. Eichenbaum, Evolution of declarative memory. *Hippocampus* **16**, 795-808 (2006).
2. M. P. Witter, T. P. Doan, B. Jacobsen, E. S. Nilssen, S. Ohara, Architecture of the Entorhinal Cortex A Review of Entorhinal Anatomy in Rodents with Some Comparative Notes. *Front. Syst. Neurosci.* **11**, 46 (2017).
3. E. I. Moser *et al.*, Grid cells and cortical representation. *Nat. Rev. Neurosci.* **15**, 466-481 (2014).
4. M. P. Witter, E. I. Moser, Spatial representation and the architecture of the entorhinal cortex. *Trends Neurosci.* **29**, 671-678 (2006).
5. K. M. Igarashi, The entorhinal map of space. *Brain Res.* **1637**, 177-187 (2016).
6. W. B. Scoville, B. Milner, Loss of recent memory after bilateral hippocampal lesions. *J. Neurol. Neurosurg. Psychiatry* **20**, 11-21 (1957).
7. B. Milner, S. Corkin, H. L. Teuber, Further analysis of the hippocampal amnesic syndrome: 14-year follow-up study of H.M. *Neuropsychologia* **6**, 215-234 (1968).
8. J. O'Keefe, J. Dostrovsky, The hippocampus as a spatial map. Preliminary evidence from unit activity in the freely-moving rat. *Brain Res.* **34**, 171-175 (1971).
9. J. O'keefe, L. Nadel, *The hippocampus as a cognitive map*. (Oxford: Clarendon Press, 1978).
10. G. Buzsaki, E. I. Moser, Memory, navigation and theta rhythm in the hippocampal-entorhinal system. *Nat. Neurosci.* **16**, 130-138 (2013).
11. N. L. M. Cappaert, N. M. Van Strien, M. P. Witter, in *The Rat Nervous System (Fourth Edition)*, G. Paxinos, Ed. (Academic Press, San Diego, 2015), pp. 511-573.
12. D. G. Amaral, M. P. Witter, The three-dimensional organization of the hippocampal formation: A review of anatomical data. *Neuroscience* **31**, 571-591 (1989).
13. V. H. Brun *et al.*, Place Cells and Place Recognition Maintained by Direct Entorhinal-Hippocampal Circuitry. *Science* **296**, 2243-2246 (2002).
14. M. Fyhn, S. Molden, M. P. Witter, E. I. Moser, M.-B. Moser, Spatial Representation in the Entorhinal Cortex. *Science* **305**, 1258-1264 (2004).
15. T. Hafting, M. Fyhn, S. Molden, M. B. Moser, E. I. Moser, Microstructure of a spatial map in the entorhinal cortex. *Nature* **436**, 801-806 (2005).
16. V. H. Brun *et al.*, Progressive increase in grid scale from dorsal to ventral medial entorhinal cortex. *Hippocampus* **18**, 1200-1212 (2008).
17. H. Stensola *et al.*, The entorhinal grid map is discretized. *Nature* **492**, 72-78 (2012).
18. V. H. Brun *et al.*, Impaired Spatial Representation in CA1 after Lesion of Direct Input from Entorhinal Cortex. *Neuron* **57**, 290-302 (2008).

19. T. Bonnevie *et al.*, Grid cells require excitatory drive from the hippocampus. *Nat. Neurosci.* **16**, 309-317 (2013).
20. J. Koenig, A. N. Linder, J. K. Leutgeb, S. Leutgeb, The Spatial Periodicity of Grid Cells Is Not Sustained During Reduced Theta Oscillations. *Science* **332**, 592-595 (2011).
21. M. P. Brandon *et al.*, Reduction of Theta Rhythm Dissociates Grid Cell Spatial Periodicity from Directional Tuning. *Science* **332**, 595-599 (2011).
22. S. S. Winter, B. J. Clark, J. S. Taube, Disruption of the head direction cell network impairs the parahippocampal grid cell signal. *Science* **347**, 870-874 (2015).
23. C. Miao, Q. Cao, M.-B. Moser, E. I. Moser, Parvalbumin and Somatostatin Interneurons Control Different Space-Coding Networks in the Medial Entorhinal Cortex. *Cell* **171**, 507-521.e517 (2017).
24. R. F. Langston *et al.*, Development of the spatial representation system in the rat. *Science* **328**, 1576-1580 (2010).
25. T. J. Wills, F. Cacucci, N. Burgess, J. O'Keefe, Development of the hippocampal cognitive map in preweanling rats. *Science* **328**, 1573-1576 (2010).
26. M. Gil *et al.*, Impaired path integration in mice with disrupted grid cell firing. *Nat. Neurosci.* **21**, 81-91 (2018).
27. M. Fyhn, T. Hafting, M. P. Witter, E. I. Moser, M. B. Moser, Grid cells in mice. *Hippocampus* **18**, 1230-1238 (2008).
28. M. M. Yartsev, M. P. Witter, N. Ulanovsky, Grid cells without theta oscillations in the entorhinal cortex of bats. *Nature* **479**, 103 (2011).
29. N. J. Killian, M. J. Jutras, E. A. Buffalo, A map of visual space in the primate entorhinal cortex. *Nature* **491**, 761 (2012).
30. J. Jacobs *et al.*, Direct recordings of grid-like neuronal activity in human spatial navigation. *Nat. Neurosci.* **16**, 1188 (2013).
31. L. M. Giocomo *et al.*, Topography of head direction cells in medial entorhinal cortex. *Curr. Biol.* **24**, 252-262 (2014).
32. F. Sargolini *et al.*, Conjunctive representation of position, direction, and velocity in entorhinal cortex. *Science* **312**, 758-762 (2006).
33. T. Solstad, C. N. Boccara, E. Kropff, M. B. Moser, E. I. Moser, Representation of geometric borders in the entorhinal cortex. *Science* **322**, 1865-1868 (2008).
34. E. Kropff, J. E. Carmichael, M. B. Moser, E. I. Moser, Speed cells in the medial entorhinal cortex. *Nature* **523**, 419-424 (2015).
35. O. A. Hoydal, E. R. Skytoen, S. O. Andersson, M. B. Moser, E. I. Moser, Object-vector coding in the medial entorhinal cortex. *Nature* **568**, 400-404 (2019).
36. L. L. Chen, L.-H. Lin, E. J. Green, C. A. Barnes, B. L. McNaughton, Head-direction cells in the rat posterior cortex. *Exp. Brain Res.* **101**, 8-23 (1994).

37. J. S. Taube, Head direction cells recorded in the anterior thalamic nuclei of freely moving rats. *J. Neurosci.* **15**, 70-86 (1995).
38. S. J. Mizumori, J. D. Williams, Directionally selective mnemonic properties of neurons in the lateral dorsal nucleus of the thalamus of rats. *J. Neurosci.* **13**, 4015-4028 (1993).
39. R. W. Stackman, J. S. Taube, Firing Properties of Rat Lateral Mammillary Single Units: Head Direction, Head Pitch, and Angular Head Velocity. *The Journal of neuroscience : the official journal of the Society for Neuroscience* **18**, 9020-9037 (1998).
40. T. L. Bjerknes, E. I. Moser, M. B. Moser, Representation of geometric borders in the developing rat. *Neuron* **82**, 71-78 (2014).
41. T. L. Bjerknes, R. F. Langston, I. U. Kruge, E. I. Moser, M. B. Moser, Coherence among head direction cells before eye opening in rat pups. *Curr. Biol.* **25**, 103-108 (2015).
42. P. Andersen, R. Morris, D. Amaral, J. O'Keefe, T. Bliss, *The hippocampus book*. (Oxford university press, 2007).
43. C. F. Doeller, C. Barry, N. Burgess, Evidence for grid cells in a human memory network. *Nature* **463**, 657-661 (2010).
44. N. K. Logothetis, The neural basis of the blood-oxygen-level-dependent functional magnetic resonance imaging signal. *Philosophical Transactions of the Royal Society B: Biological Sciences* **357**, 1003-1037 (2002).
45. D. J. Heeger, D. Ress, What does fMRI tell us about neuronal activity? *Nature Reviews Neuroscience* **3**, 142 (2002).
46. C. Stippich, Clinical functional MRI: presurgical functional neuroimaging. (Springer, 2015).
47. N. K. Logothetis, J. Pauls, M. Augath, T. Trinath, A. Oeltermann, Neurophysiological investigation of the basis of the fMRI signal. *Nature* **412**, 150 (2001).
48. J. B. M. Goense, N. K. Logothetis, Neurophysiology of the BOLD fMRI Signal in Awake Monkeys. *Curr. Biol.* **18**, 631-640 (2008).
49. D. Hermes, M. Nguyen, J. Winawer, Neuronal synchrony and the relation between the blood-oxygen-level dependent response and the local field potential. *PLoS Biol.* **15**, e2001461 (2017).
50. K. Schulz *et al.*, Simultaneous BOLD fMRI and fiber-optic calcium recording in rat neocortex. *Nature Methods* **9**, 597 (2012).
51. A. T. Winder, C. Echagarruga, Q. Zhang, P. J. Drew, Weak correlations between hemodynamic signals and ongoing neural activity during the resting state. *Nat. Neurosci.* **20**, 1761-1769 (2017).
52. Aidan J. Horner, James A. Bisby, E. Zotow, D. Bush, N. Burgess, Grid-like Processing of Imagined Navigation. *Curr. Biol.* **26**, 842-847 (2016).
53. M. Nau, T. Navarro Schröder, J. L. S. Bellmund, C. F. Doeller, Hexadirectional coding of visual space in human entorhinal cortex. *Nat. Neurosci.* **21**, 188-190 (2018).

54. L. Kunz *et al.*, Reduced grid-cell–like representations in adults at genetic risk for Alzheimer's disease. *Science* **350**, 430 (2015).
55. J. L. S. Bellmund, L. Deuker, T. Navarro Schröder, C. F. Doeller, Grid-cell representations in mental simulation. *eLife* **5**, e17089 (2016).
56. A. O. Constantinescu, J. X. O'Reilly, T. E. J. Behrens, Organizing conceptual knowledge in humans with a gridlike code. *Science* **352**, 1464-1468 (2016).
57. T. Stensola, H. Stensola, M. B. Moser, E. I. Moser, Shearing-induced asymmetry in entorhinal grid cells. *Nature* **518**, 207-212 (2015).

NTNU

Kunnskap for ei betre verd